A System for Detecting the Position of a Molten Aluminum Metal-Front within a Precision Sand Mold

By

Brian M. Foley

A Thesis

Submitted to the Faculty

of the

WORCESTER POLYTECHNIC INSTITUTE

in Partial Fulfillment of the Requirements for the

Degree of Master of Science

in

Electrical and Computer Engineering

_____

Brian M. Foley

September 2008

Approved:

_____   _____

Dr. Reinhold Ludwig, Major Advisor   Dr. Hossein Hakim, ECE Dept.

_____

Scott W. Biederman, GM Powertrain

Table of Contents

Table of Figures

Table of Tables

Abstract

Manufacturers of cast metal parts are interested in the development of a feedback control system for use with the Precision Sand-Casting (PSC) process. As industry demands the ability to cast more complex geometries, there are a variety of challenges that engineers have to address. Certain characteristics of the mold, such as thick-to-thin transitions, extensive horizontal or flat surfaces, and sharp corners increase the likelihood of generating defective casts due to the turbulent metal-flow during fills. Consequently, it is critical that turbulent flow behavior within the mold be minimized as much as possible.

One way to enhance the quality of the fill process is to adjust the flow rate of the molten metal as it fills these critical regions of the mold. Existing systems attempt to predict the position of the metal level based on elapsed time from the beginning of the fill stage. Unfortunately, variability in several aspects of the fill process makes it very difficult to consistently predict the position of the metal front. A better approach would be to imbed a sensor that can detect the melt through a lift-off distance and determine the position of the metal-front. The information from this sensor can then be used to adjust the flow rate of the aluminum as the mold is filled.

This thesis presents the design of a novel non-invasive sensor monitoring system. When deployed on the factory floor, the sensing system will provide all necessary information to allow process engineers to adjust the metal flow-rate within the mold and thereby reduce the amount of scrap being produced. Moreover, the system will exhibit additional value in the research and development of future mold designs.

Acknowledgements

I would like to begin by thanking Scott Biederman of General Motors for his dedication to this project. The support and mentorship provided by Mr. Biederman has had a profound influence on me, for which I will be eternally grateful. In conjunction, I would also like to thank the amazing team of engineers and technicians at Metal Casting Technology, Inc. (MCT) for taking the time to teach me about their field and making me feel so welcome at their facility. I would also like to acknowledge the contribution of retired MCT President, Paul Mikkola, whose desire for innovation was a critical component in getting this project off the ground.

I would like to thank my thesis advisor, Professor Reinhold Ludwig, for his guidance and patience throughout the many twists and turns along the development process for this system. I would also like to thank Professor Sergey Makarov for offering a helping hand whenever needed, as well as Professor Hossein Hakim for being a member of my defense committee.

Last but not least, I would like to thank my parents, Jack and Robin Foley, as well as my sisters, Lindsay and Mara, for their unconditional love and support throughout this chapter of my lifetime.

1 Problem Statement

Casting producers in the automotive industry are faced with several engineering challenges regarding the production of cast aluminum engine blocks. Due to the complex design of a modern engine block, it is very difficult to produce a part with such a complicated geometry by material-removal processes. As an alternative, it is often easier to employ a material-forming process to manufacture such intricate parts. One option for creating parts like engine blocks is Precision Sand Casting (PSC) [1]. Precision sand casting (PSC) is a material forming process capable of producing parts with complex geometries that exhibit excellent mechanical properties, dimensional precision, and good surface finish. As a result, PSC has been employed extensively by the aerospace and automotive industries in applications with significant structural demands.

As an example, PSC makes it possible to cast an aluminum engine block while maintaining sufficient dimensional accuracy as compared to producing the same part through machining processes. In production, the sand mold for the engine block shape is composed of several individual pieces called cores. Figure 1.1 is a photo of an engine block mold that has been partially disassembled to show some of these cores.

Figure 1.1: Partially disassembled core package for an eight-cylinder, v-block engine

The cores are carefully assembled by several industrial robots and inspected frequently to ensure that the cores remain intact and fit together tightly. Once the sand mold has been fully

assembled, molten aluminum is injected into the mold by a pumping system at a rate of approximately 5 to 7.5 lbs/second. After the metal within the mold has been given time to solidify, the sand is broken away to reveal the cast aluminum engine block.

For all the advantages of PSC, there are still many challenges that metallurgists and process engineers must address to consistently produce quality castings. Several of these challenges arise from the complexity of the parts being cast through PSC. As an example, current engine blocks include several design aspects that can make them very difficult to cast, including thin metal walls and large volume transitions. Figure 1.2 identifies one such instance of extreme volume-transition on the engine block; the point at which the skirts (outlined in yellow) branch from the bulk of the engine block. This location presents a significant problem because when molten aluminum is being pumped at a high flow rate to fill the bulk of the part and then reaches the reduced volume of the skirts, the result is a significant increase in metal velocity. This high velocity can cause several problems, including metal penetration into the walls of the mold or the dislodging of the sand within the cavity, resulting in scrap parts [1], [2].
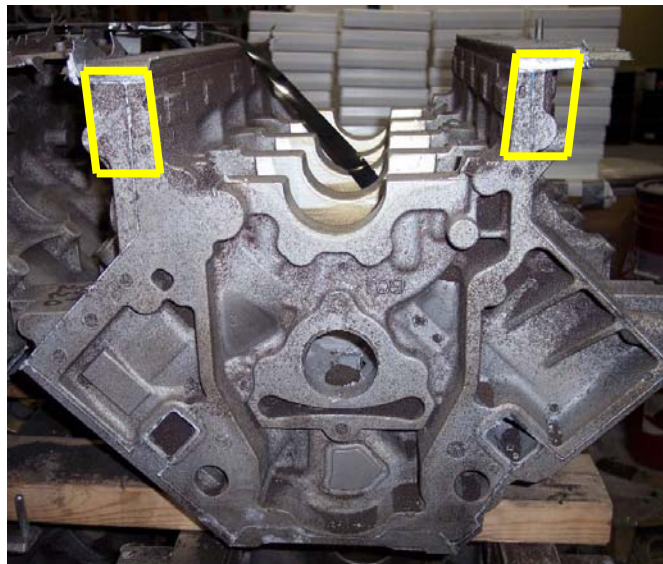
Figure 1.2: Side profile of a V-block engine with skirt areas highlighted

Problems such as these could be avoided if the flow-rate of the molten aluminum through these regions could be adjusted as necessary. The problem in implementing this strategy is that it is very difficult to know or predict where the molten aluminum is within a sand mold at any time. For one thing, it is impossible to monitor the process visually since the cavity is completely encased in sand. Efforts have been made in the past to adjust metal flow-rate based

on elapsed time. However, several elements of the process, including the variable permeability of the molds, melt temperature and the working condition of the melt delivery system are too inconsistent from pour to pour to accurately predict the location of the metal front based solely on time.

Therefore, the goal of this project was to create a system that could accurately determine the position of an aluminum molten-metal front within a sand mold and do so consistently despite the aforementioned sources of variability. Such a system would provide the necessary information to allow process engineers to adjust the metal flow-rate within the mold and reduce the amount of scrap being produced. The system could exhibit additional value in the research and development of future mold designs as a tool used to validate theoretical models of molds being filled with molten metal.

2 Background

This section will provide background information about eddy current testing. Additionally, it will also formulate the theory behind the induction of eddy-currents in a conductive material and the operation of a tuned-circuit oscillator.

2.1 Eddy Current Application

Eddy current testing (ECT) is an ideal inspection technique for electrically conducting media. An eddy current is the circular flow of electric charge within a conductive medium that arises in response to the presence of a time-varying (AC) magnetic field. The behavior of these eddy currents is directly related to the material properties of the domain in which they exist. By controlling the application of the AC magnetic field, these eddy currents can provide valuable information about a metallic material, including its surface hardness and the presence of any corrosion or defects both on and below the surface. As a result, ECT has established itself in several manufacturing markets as a proven method for the non-destructive evaluation (NDE) of metal components, including the automotive and aircraft industries in particular [3], [4].

The existence of eddy currents was first demonstrated by Jean-Bernard Léon Foucault in 1830. Foucault showed that when a conductor is moved within a constant (static) magnetic field, eddy currents are generated in the conductor and provide a force that opposes the conductor's direction of motion. The actual experiment that demonstrated this consisted of a copper disc rotating within a static magnetic field and Foucault observed that as the number of revolutions per minute (RPM) of the disc was increased, the applied force required to maintain the targeted RPM increased as well due to the retarding force generated by the eddy currents [4].

To complement the work of Foucault, the discovery that eddy currents can be generated within a stationary conductor when subjected to a changing magnetic field stemmed from the independent discovery of electromagnetic induction by Michael Faraday and Joseph Henry in 1831. The phenomenon arose from their observations that the AC magnetic field of an excitation source (called the *primary coil*) creates an electromotive force (EMF) within a nearby conductor (called the *secondary coil*) located in the vicinity of the primary coil. Furthermore, if a load is connected across the terminals of the secondary to create a closed circuit, a current will flow

4

within this circuit to generate a secondary magnetic field whose magnitude is equal to that of the primary, but with a phase difference of 180° [3], [7].

The principles of electromagnetic induction can be applied to explain the generation of eddy currents in a stationary conductor. What if the conductor that comprises the secondary in the aforementioned system is a sheet of metal instead of a wire? An EMF will still be generated in the sheet of metal due to the AC magnetic field from the primary, and electric currents will flow in closed loops (called eddys) across the surface of the sheet. The distributed nature of the induced eddy currents present in the sheet can be thought of as a transformer with several secondary components, all of which are connected to a load that represents the resistivity of the metallic material. The superposition of the secondary magnetic fields produced by these eddys produces a total field that opposes the primary field in magnitude and phase [7].

The nature of eddy currents generated by electromagnetic induction makes ECT a very powerful technique in evaluating metallic components for several reasons. First, ECT is a non-contacting inspection technique, meaning that the excitation source and the test specimen are not in physical contact with one another. Second, eddy currents can only arise within conductive materials and cannot exist in high-resistivity materials such as wood, concrete, ceramics, plastics, silica, etc. The result of these two qualities is that ECT is ideally suited for applications involving the inspection of metals where the excitation source (called the probe) and metallic sample are separated by one of these high-resistivity materials mentioned earlier. These materials will not distort the AC magnetic field generated by the probe, allowing the field from the source to interact with the metallic specimen as if they were separated by air [5].

It is this characteristic of ECT that makes it an ideal technique for the detection of aluminum within a precision sand mold. Because the sand is one of these high-resistivity materials, we can expect that the AC magnetic field of a probe placed on the outer surface of the mold will be able to interact with the aluminum, generating eddy currents within the melt as it fills the mold.

ECT encompasses a variety of ways to detect the effect of the eddy currents on the total magnetic field. One approach is to use separate pickup probes around the primary probe and monitor induced voltages to detect changes in the magnetic field. Another is to use the primary probe as a transceiver (transmitter and receiver) and monitor its impedance for changes that can be correlated to the interactions between the primary and the test specimen. While the former

technique requires less sophisticated circuitry to generate the AC magnetic field and detect changes in voltages of the pickup probes, it also requires more total components to comprise the system. Conversely, the latter technique involves only a single probe, but also requires a more complex circuit design that will both drive the probe and detect the most minute changes in its impedance [3] [4].

2.2 Eddy Currents

Eddy current phenomena can be described mathematically through the combination of Maxwell's equations and the appropriate boundary conditions for the solution space of interest. The necessary equations include Ampére's law

$$\nabla \times \mathbf{B} = \mu \mathbf{J}_{total} + \mu \varepsilon \frac{\partial \mathbf{E}}{\partial t} \tag{2.1}$$

Faraday's law,

$$\nabla \times \mathbf{E} = -\frac{\partial \mathbf{B}}{\partial t} \tag{2.2}$$

Gauss's equation,

$$\nabla \cdot \mathbf{E} = \frac{\rho}{\varepsilon} \tag{2.3}$$

and the divergence of the magnetic flux density, $\mathbf{B}$,

$$\nabla \cdot \mathbf{B} = 0 \tag{2.4}$$

where $\mathbf{J}_{total}$ is the total current density present in the system, ρ is the free charge in the system, μ and σ are the material-dependent permeability and conductivity and ε is equal to the permittivity of free space. $\mathbf{J}_{total}$ is the sum of the impressed current density within the probe coil, $\mathbf{J}_s$, and the induced eddy current density, $\mathbf{J}_e$, within the targeted region

$$\mathbf{J}_{total} = \mathbf{J}_s + \mathbf{J}_e \tag{2.5}$$

Additionally, $\mathbf{J_e}$ is related to the induced electric field, $\mathbf{E}$, within the target region by Ohm's law

$$\mathbf{J_e} = \sigma\mathbf{E} \tag{2.6}$$

Substitution of (2.5) and (2.6) into (2.1) yields

$$\nabla \times \mathbf{B} = \mu\mathbf{J_s} + \mu\sigma\mathbf{E} + \mu\varepsilon\frac{\partial\mathbf{E}}{\partial t} \tag{2.7}$$

The coupled relationship between $\mathbf{B}$ and $\mathbf{E}$ can be simplified through the introduction of the magnetic vector potential, $\mathbf{A}$, and the electric scalar potential, ϕ. The inclusion of these concepts helps us decouple the relationship between $\mathbf{B}$ and $\mathbf{E}$ and express the behavior of the eddy currents in terms of these potentials. As shown further below, once the solution has been obtained in terms of $\mathbf{A}$ or ϕ, $\mathbf{B}$ and $\mathbf{E}$ can be calculated from these potentials.

Because of the solenoidal nature of the magnetic field described by (2.4), we can express the magnetic flux density, $\mathbf{B}$, as the curl of another vector. This vector is the magnetic vector potential, $\mathbf{A}$, and the relationship between $\mathbf{A}$ and $\mathbf{B}$ is

$$\nabla \times \mathbf{A} = \mathbf{B} \tag{2.8}$$

To define the electric scalar potential, ϕ, we substitute (2.8) into (2.2) and rearrange to produce

$$\nabla \times \left(\mathbf{E} + \frac{\partial\mathbf{A}}{\partial t}\right) = \mathbf{0} \tag{2.9}$$

Here, the combined vector field in the bracket is an expression for a conservative vector field. Because of this, the expression within the parenthesis in (2.9) can be set equal to the negative divergence of a scalar field, ϕ, to eventually yield an expression for $\mathbf{E}$ in terms of ϕ and $\mathbf{A}$;

$$\mathbf{E} = -\nabla\phi - \frac{\partial\mathbf{A}}{\partial t} \tag{2.10}$$

We can now modify (2.7) and (2.3) by substituting (2.8) and (2.10). This yields two expressions

$$\nabla \times \nabla \times \mathbf{A} + \mu\sigma\frac{\partial \mathbf{A}}{\partial t} + \mu\varepsilon\frac{\partial^2 \mathbf{A}}{\partial t^2} = \mu\mathbf{J}_\mathrm{s} - \mu\sigma\nabla\phi - \mu\varepsilon\nabla\frac{\partial\phi}{\partial t} \tag{2.11}$$

and

$$-\frac{\partial}{\partial t}(\nabla \cdot \mathbf{A}) = \frac{\rho}{\varepsilon} + \nabla^2\phi \tag{2.12}$$

The double curl operation on **A** can be re-written with the following identity

$$\nabla \times \nabla \times \mathbf{A} = \nabla(\nabla \cdot \mathbf{A}) - \nabla^2\mathbf{A} \tag{2.13}$$

resulting in

$$\nabla(\nabla \cdot \mathbf{A}) - \nabla^2\mathbf{A} + \mu\sigma\frac{\partial \mathbf{A}}{\partial t} + \mu\varepsilon\frac{\partial^2 \mathbf{A}}{\partial t^2} = \mu\mathbf{J}_\mathrm{s} - \mu\sigma\nabla\phi - \mu\varepsilon\nabla\frac{\partial\phi}{\partial t} \tag{2.14}$$

Finally, if we define the divergence of **A** through the Lorentz gauge for lossy materials

$$\nabla \cdot \mathbf{A} = -\mu\sigma\phi - \mu\varepsilon\frac{\partial\phi}{\partial t} \tag{2.15}$$

and apply (2.15) to both (2.14) and (2.12), the result is two separate equations that define an eddy current system

$$-\nabla^2\mathbf{A} + \mu\varepsilon\frac{\partial^2 \mathbf{A}}{\partial t^2} + \mu\sigma\frac{\partial \mathbf{A}}{\partial t} = \mu\mathbf{J}_\mathrm{s} \tag{2.16}$$

$$-\nabla^2\phi + \mu\varepsilon\frac{\partial^2 \phi}{\partial t^2} + \mu\sigma\frac{\partial\phi}{\partial t} = \frac{\rho}{\varepsilon} \tag{2.17}$$

Since we are primarily interested in the magnetic vector potential due to the excitation current density, $\mathbf{J}_\mathrm{s}$, we would like to find a solution for (2.16). If we assume that the $\mathbf{J}_\mathrm{s}$ is sinusoidal and of the form

$$\mathbf{J}_\mathrm{s} = \alpha e^{j\omega t} \tag{2.18}$$

where α is the amplitude of the sinusoid and ω is its frequency in radians per second. Consequently, **A** will also be sinusoidal due to the linearity of the system and each of the first and second derivatives with respect to time in (2.16) can be replaced with $j\omega$ and $-\omega^2$, respectively. These substitutions yield

$$\nabla^2 \mathbf{A} + \omega^2 \mu\varepsilon\mathbf{A} - j\omega\mu\sigma\mathbf{A} = -\mu\mathbf{J}_s \qquad (2.19)$$

In many eddy current testing applications, the frequency of the sinusoidal excitation current, f, is usually less than 500 kHz. Additionally, typical conductivities (σ) of test specimens are often larger than 0.5e7 S/m. The result of these observations is that the magnitude of the imaginary part in (2.19) will dominate the magnitude of the real part. Therefore, the real part is omitted for low frequencies, and (2.19) becomes an elliptical equation

$$\nabla^2 \mathbf{A} - j\omega\mu\sigma\mathbf{A} = -\mu\mathbf{J}_s \qquad (2.20)$$

The final step is to employ one of several possible numerical techniques, including the finite element method (FEM) or finite-differences time-domain (FDTD), to determine the values of **A** for discrete points within the solution space. In most cases, the type of numerical solution will be dictated by the nature of the geometries in the solution space, with the FDTD being best suited for regular, flat geometries and FEM being idea for irregular geometries and curves.

Once the values of **A** are known, they can then be used to calculate the impedance of the probe coil, Z, by integrating the dot product of **A** along the path of the wire in the probe coil and scaling the result by $j\omega/I$, in accordance with the following expression

$$Z = \frac{j\omega}{I}\left(\oint_{wire} \mathbf{A} \cdot dl \right) \qquad (2.21)$$

Therefore, if the value of the magnetic vector potential at the probe terminals is perturbed by the presence of a nearby metal target, we will ultimately observe a change in the impedance of the probe [8].

From a practical standpoint, the impedance of the probe is something that we can actually measure, as opposed to the magnetic vector potential which is a fictitious quantity altogether. One way to perform this measurement is to design an oscillator that is sensitive to changes in this impedance so that any changes in the reactive part will produce a shift in the natural frequency of the oscillator that can be measured [9], [10].

2.3 Oscillator

To enable the detection of the most minute changes in probe impedance due to the presence of molten aluminum, a tuned-circuit oscillator was selected as the drive circuit topology for the system. The idea was that by using the probe as the inductance in an LC tuning circuit, any changes in inductance due to the presence of molten aluminum would cause a shift in the natural frequency of the oscillator. If the oscillator could be designed to remain stable over a range of operating conditions, and yield adequate resolution, it would provide a very simple and inexpensive means of detecting the position of the molten aluminum.

The basic representation of a feedback oscillator is pictured in Figure 2.1. The diagram encompasses three primary blocks: (1) an Amplifier, A, (2) an amplitude-limiting mechanism, L(v), and (3) a frequency-determining network, $\beta(\omega)$.
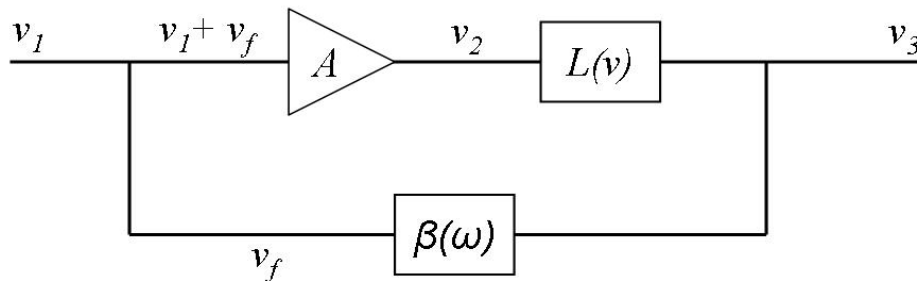

Figure 2.1: System diagram of the feedback oscillator

The closed-loop gain of the above system is given by combining the equations describing the forward-gain transmission and the feedback voltage. Equation (2.22) defines the closed-loop gain, G, to be:

$$G = \frac{v_3}{v_1} = \frac{A \cdot L(v)}{1 - A \cdot L(v) \cdot \beta(\omega)} \qquad (2.22)$$

If the oscillations are to be self-sustaining, there must be an output response with no input excitation ($v_1 = 0$). This means that the denominator in equation (2.22) must be equal to zero and that the feedback must be regenerative. The expression for this condition is given in equation (2.23) below and we can see that in order for this to be true, the open-loop transmission ($A*L(v)*\beta(\omega)$) must be equal to unity, implying that whatever is present at the start of the loop returns unaffected at the end [11].

$$v_1 = 1 - A \cdot L(v) \cdot \beta(\omega) = 0 \qquad (2.23)$$

In the case of small signals where the limiting factor is assumed insignificant ($L(v) \approx 1$), the result is a simplified version of the Barkhausen criterion for oscillation given in equation (2.24).

$$A \cdot \beta(\omega) = 1 \qquad (2.24)$$

$$\beta(\omega) = \beta_R(\omega) + j\beta_i(\omega) \qquad (2.25)$$

Because the frequency-determining network described by $\beta(\omega)$ is comprised of reactive components and yields complex-conjugate roots, the left-hand side of equation (2.24) has both a real part and an imaginary part, as seen in equation (2.25). To satisfy Equation (2.24), the imaginary part must be equal to zero. It is this frequency, ω, where $\beta_i = 0$ at which the tuned circuit will oscillate [11].

To physically realize this feedback oscillator, we need to choose the amplifier element (A) for the system, as well as the topology of the feedback network ($\beta(\omega)$). Several combinations of amplifier elements and feedback networks have been thoroughly investigated, each with their share of benefits and detriments associated with their implementation. These combinations are delineated primarily by their different feedback networks, as most amplifier elements are universally applicable.

The feedback networks are comprised of some combination of inductors and capacitors to provide the series or parallel resonant condition required. What is unique about these combinations are where the networks are tapped to provide the feedback in the system. Two of

the best examples of this are the Hartley oscillator and the Colpitts oscillator. The feedback networks of these two circuits are pictured in Figure 2.2.
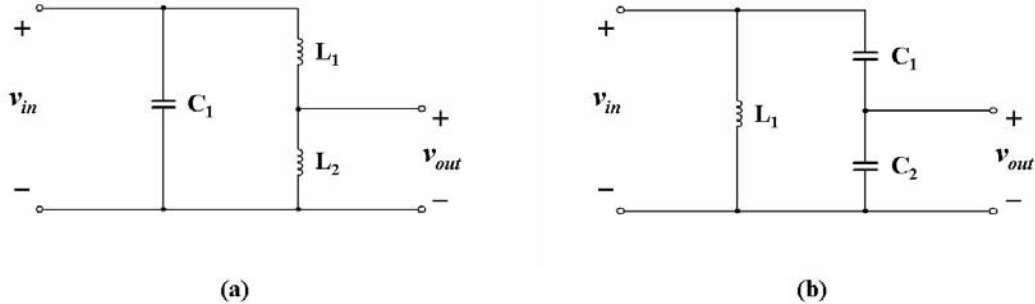
Figure 2.2: The Hartley (a) and Colpitts (b) frequency-selective networks

The Hartley network consists of two inductors (or a single, center-tapped inductor) and a single capacitor. In this circuit, the feedback to the amplifier is tapped at the node between the two inductors. On the other hand, the Colpitts network encompasses a single inductor and two capacitors with the feedback being tapped from the node between the capacitors.

Because the probe coil in our system is essentially an inductor, and we are interested in the affect of the molten aluminum on the inductance of the coil, the Colpitts topology was selected for the feedback network. Choosing the network containing a single inductor guarantees that any change in the inductive leg of the network is due to the probe coil and not a secondary inductor as might be the case with the Hartley topology.

Having chosen the feedback network, the next step is to choose the amplification element, A, in the feedback system. Two of the more common choices for this amplification are the Bipolar Junction Transistor (BJT) and the Metal-Oxide Semiconductor Field Effect Transistor (MOSFET). For this design, the BJT was selected for a specific reason concerning the small-signal model of the MOSFET. Figure 2.3 shows the small-signal transistor model of both the MOSFET and the BJT for frequencies less than 200 kHz (at higher frequencies, several additional parasitic capacitances must be included).
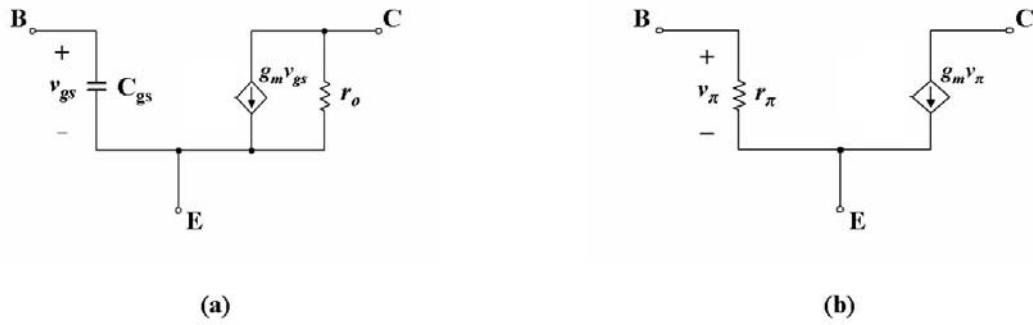
Figure 2.3: Low frequency small-signal models for the MOSFET (a) and the BJT (b)

As we can see in Figure 2.3, the input (gate) of the MOSFET is modeled as a Gate-to-Source capacitance (C_{GS}) where as the input to the BJT is a resistor (r_π). The problem with the MOSFET is that this capacitive input can affect the total capacitance of the feedback network, ultimately causing the natural frequency of the oscillator to drift during operation. It is very important that the steady-state behavior of the oscillator be as stable as possible, and it is for this reason that the BJT was selected for our feedback oscillator.

The feedback network and BJT were combined to yield the common-base Colpitts oscillator circuit pictured in Figure 2.4.
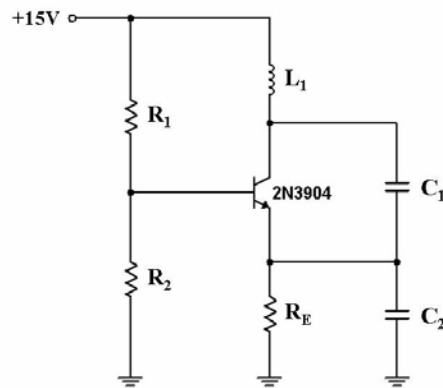
Figure 2.4: Common-base Colpitts oscillator circuit

In this design, the feedback from the Colpitts network is routed to the emitter terminal of the BJT. If we substitute the BJT small-signal model from Figure 2.3(b) into the oscillator circuit, the result is the small-signal equivalent circuit pictured in Figure 2.5.
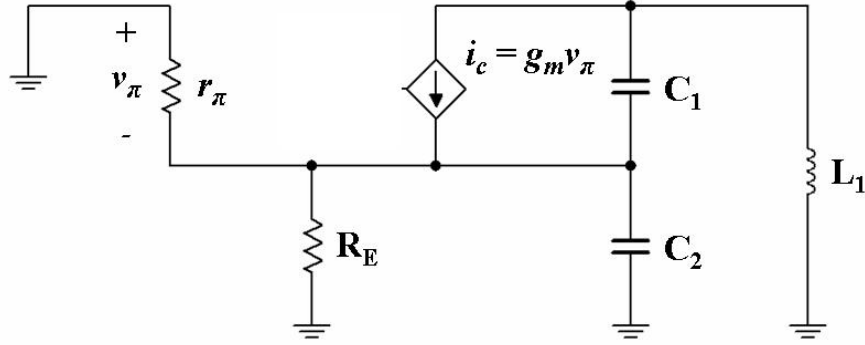
Figure 2.5: Small-signal model of the common-base Colpitts oscillator

To define the new circuit element, r_π, we need to calculate the transconductance, g_m, of the BJT given by

$$g_m = \frac{I_C}{V_T} \qquad (2.26)$$

where I_C is the bias collector current from the large signal model and V_T is the thermal voltage (at room temperature, $V_T \approx 26\text{mV}$).

Using the value of g_m, we then calculate r_π from

$$r_\pi = \frac{h_{fe}}{g_m} \qquad (2.27)$$

where h_{fe} is the small-signal current gain of the transistor obtained from the datasheet. Furthermore, we can calculate the small-signal collector current, i_c, from

$$i_c = g_m v_\pi \qquad (2.28)$$

where v_π is the voltage across the resistor, r_π.

If we combine r_π and R_E into a parallel equivalent resistance, R, and replace the reactive elements with generalized impedance elements ($C_1 \rightarrow Z_1$, $C_2 \rightarrow Z_2$, $L_1 \rightarrow Z_3$), we can apply Kirchhoff's laws to the circuit in Figure 2.5 to produce the following system of equations

14

$$(Z_1 + Z_2 + Z_3) \cdot i_1 + (g_m R Z_1 - Z_2) \cdot i_2 = 0 \qquad (2.29)$$

$$(-Z_2) \cdot i_1 + (R + Z_2) \cdot i_2 = 0 \qquad (2.30)$$

If we put this system of equations into matrix form and find the system determinant, we can then produce an expression for the natural frequency of the oscillator by setting the imaginary terms of the determinant equal to zero and solving for ω. The determinant of this system is given as

$$\Delta = Z_1 Z_2 \cdot (1 + g_m R) + Z_1 Z_3 + R \cdot (Z_1 + Z_2 + Z_3) \qquad (2.31)$$

Assuming that the impedances of Z_1, Z_2 and Z_3 are all purely reactive, the imaginary part of the system determinant is given by

$$R \cdot (Z_1 + Z_2 + Z_3) = 0 \qquad (2.32)$$

where

$$Z_1 = \frac{1}{j\omega C_1} \qquad (2.33)$$

$$Z_2 = \frac{1}{j\omega C_2} \qquad (2.34)$$

$$Z_3 = j\omega L \qquad (2.35)$$

By substituting (2.33)-(2.35) into (2.32) and solving for ω, the result is

$$\omega_o = \sqrt{\frac{C_1 + C_2}{L C_1 C_2}} = \frac{1}{\sqrt{L C_{parallel}}}; C_{parallel} = \frac{C_1 C_2}{C_1 + C_2} \qquad (2.36)$$

We can now see that if the inductance of the probe changes due to the presence of the moving metal front, the result will be a shift in the natural frequency of the oscillator that can be measured and ultimately related to metal-front position.

Furthermore, we can also determine the gain requirements of the oscillator by setting the real part of the determinant in equation (2.31) equal to zero and substituting (2.33)-(2.35), which (after rearranging terms) results in

$$\omega^2 L C_2 - g_m R = 1 \tag{2.37}$$

If we substitute equation (2.36) into equation (2.37) and rearrange the terms once again, the result is an expression for the appropriate ratio of capacitances C_1 and C_2 based on the transconductance of the transistor amplifier. This expression is given by

$$\frac{C_2}{C_1} \le g_m R \tag{2.38}$$

A complete derivation of the expressions for the natural frequency and gain requirements for this Colpitts oscillator is provided in Appendix A [11], [12], [13].

3 System Design

Figure 3.1 is a block diagram of the system created to meet the design objectives. As the sand mold is filled with aluminum, the coupling between the coil and the melt changes the inductance of the coil. Within the circuit-portion of the system, this change in inductance affects the natural frequency of the oscillator circuit according to (2.36). In turn, the shift in frequency is converted to a change in DC voltage and is logged by a Data Acquisition (DAQ) system for further processing via a computer.
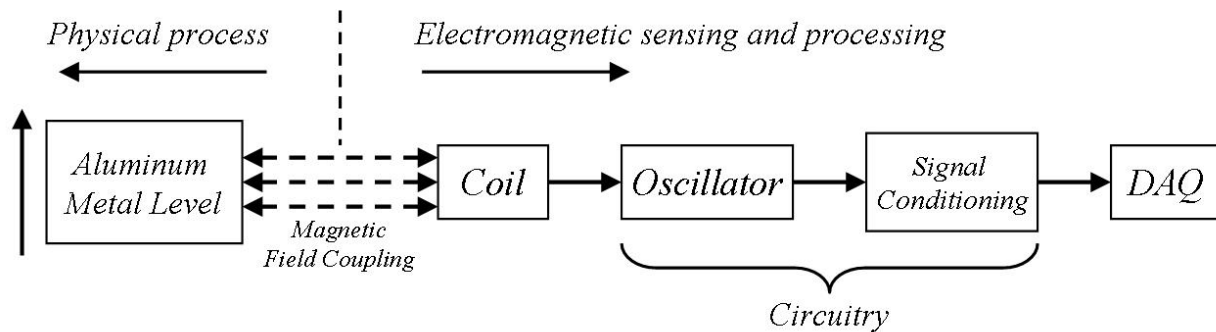
Figure 3.1: System block diagram of the melt-level monitoring system

The sub-sections to follow will detail the design and operation of each block in this system diagram.

3.1 Coil Design

A system that can be deployed on the production lines with minimal impact on the existing process (ie, redesign or relocation of components on the existing casting apparatus) is required. The ideal situation would be to have the sensor on a pneumatic actuator that would bring the coil to the surface of the mold when ready to cast the part. Additionally, the coil must be located in an area only four inches deep, meaning that the coil cannot be longer than a few inches.

In accordance with the sponsor's design constraints, a six inch (6") diameter ring was the selected geometry for the sensing coil. The ring geometry was chosen instead of a more

sophisticated geometry to facilitate quick fabrication and expedite the development of the system circuitry.

Figure 3.2 shows both a 3D CAD drawing of the former and a photo of the actual coil. The former is made out of grey PVC plastic and consists of two pieces: (1) the primary section upon which the windings of the coil are located, and (2) a removable ring that shields the windings of the coil from the environment when the sensor is deployed. The ring is fastened to the former by eight nylon screws. Non-conductive materials were selected for both the former and the fasteners to minimize possible distortions of the magnetic field pattern due to eddy current generation in the conductive materials.
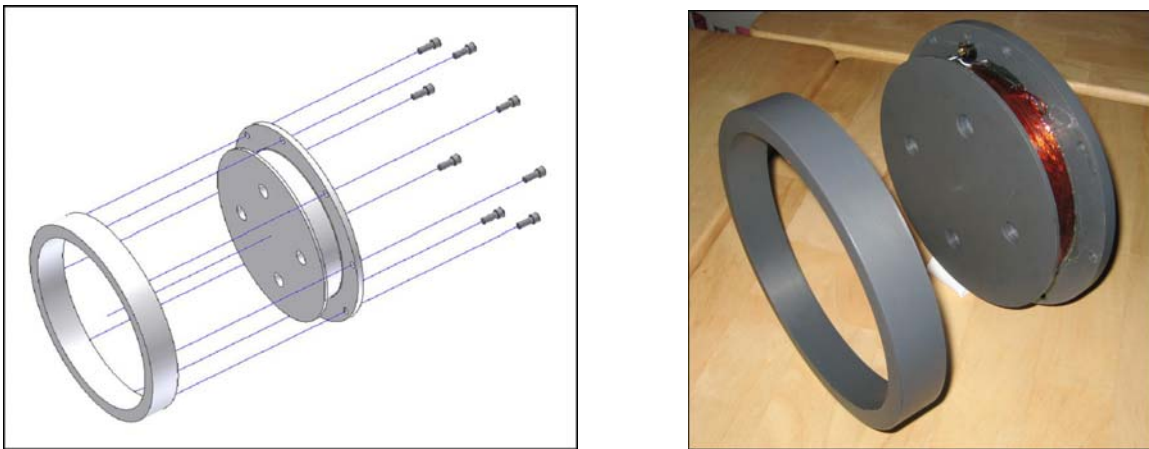
Figure 3.2: 3D CAD model and actual photo of the ring coil

The coil is six inches (6") in diameter, one inch (1") in length and is wound with 16-AWG wire. There are two layers of windings with each layer consisting of 16 turns, resulting in a total of 32 turns. The measured electrical characteristics of this coil are summarized in Table 3.1.

Table 3.1: Electrical characteristics of ring coil, measured with an LCR meter at three different test frequencies

Frequency, f (kHz)	Series Inductance, L_s (μH)	Series Resistance, R_s (Ω)	Quality factor, Q
1	284.95	0.491	3.6
10	284.41	0.655	27.3
100	309.87	4.593	42.3

As an AC current flows through its windings, an alternating magnetic field is created in the space surrounding the coil. As explained in the background, it is the interaction of this changing magnetic field with the molten metal that is central to the system's behavior. In our case, the AC current is sinusoidal which means that the behavior of the coil's magnetic field is sinusoidal as well.

Figure 3.3 is comprised of several images from an electromagnetic simulation product called Maxwell 3D (Ansoft Corporation). The structure being simulated is the 6" diameter, ring coil geometry wound on a PVC former that is pictured in Figure 3.3a. Maxwell 3D employs a Finite Element Method (FEM) solver which divides the solution space into a multitude of much smaller elements called tetrahedra, collectively referred to as a mesh. Boundary conditions for the various structures in the solution space are then applied to these tetrahedral and an iterative numeric method is carried out to calculate the field quantities of interest. The goal of this iterative method is to minimize the error between the expected total energy in the system (obtained from the excitation source(s) assigned to the structure) and the actual total energy calculated from the sum of the individual tetrahedral.
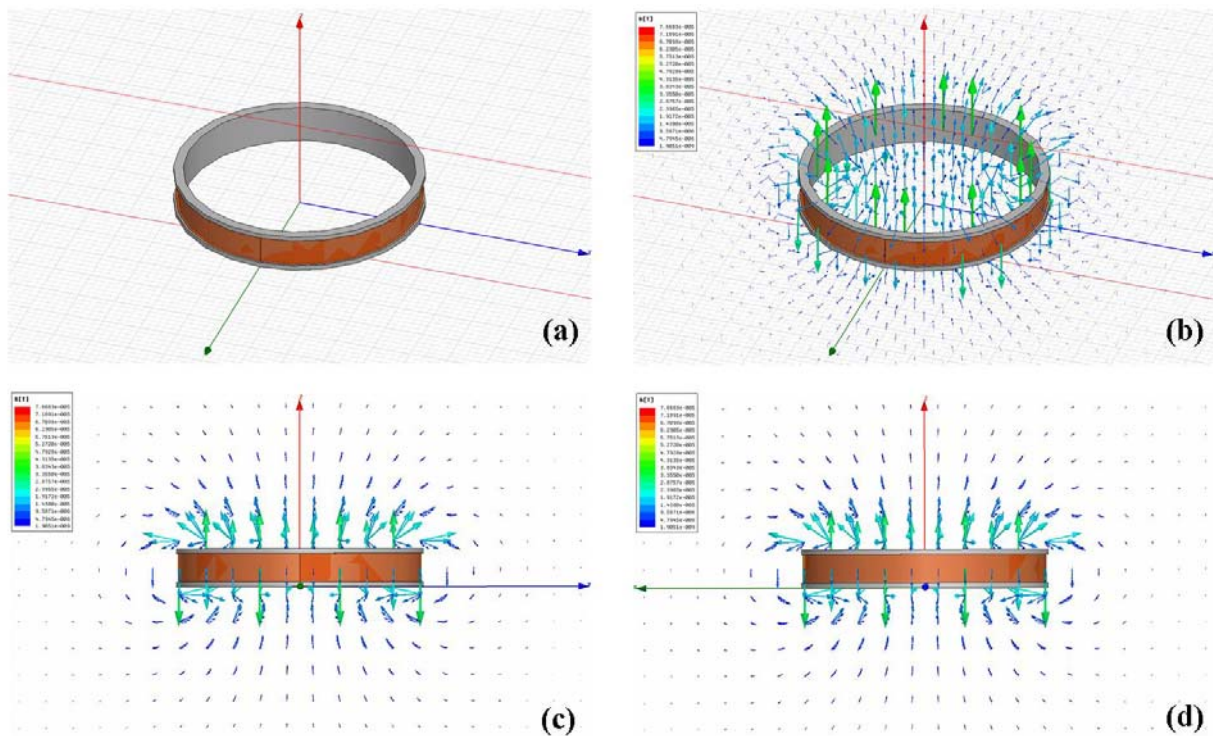

Figure 3.3: B-field plots of 6" dia. ring coil, excited by a 75kHz sinusoid with 1.12 A·turns amplitude

When using an FEM solver to simulate a particular system, structural and material boundaries often require extensive mesh refinements (decreasing the size of the local tetrahedral) to accurately determine the field quantities in these regions. Due to this face, the coil structure pictured in Figure 3.3a is that of a single, solid copper ring instead of 32 individual windings of copper wire. The reason for doing this is that if a 32 turn coil structure was simulated, the software would generate an extremely fine mesh in the regions between adjacent windings. Since a finer mesh requires a larger amount of computing resources (memory, CPU speed), a 32 turn structure would take weeks to accurately simulate, and would probably crash the computer. Therefore, the better option is the single ring structure where the current excitation is set as the peak amplitude of the AC current through the coil multiplied by the 32 turns. The result is that the single ring will represent the superposition of 32 identical loops of wire, all driven by the same current.

The specific parameters for the current excitation were that the coil would be driven by a 75kHz sinusoid with an RMS amplitude of 1.12 ampere-turns (32 turns multiplied by 35mA, determined through simulation to be the expected RMS current passing through the coil) and an initial direction counter-clockwise with respect to the positive z-axis. The simulation was configured to stop upon reaching 0.0001 percent error or after 15 iterations, whichever comes first. For each iteration, the number of tetrahedra in the mesh would be increased by 30%. Figures 3.3b, 3.3c and 3.3d are vector plots of the magnetic flux density, B, in the region surrounding the coil structure. The plots illustrate some important characteristics of the B-field from a ring coil structure, specifically the fact that the field is directionally uniform in the region between the windings and diverges from the axis of the coil in the positive z-direction. The resulting pattern is called the magnetic dipole pattern due to its similarity to that of a rectangular, permanent bar magnet.

In conjunction with this field pattern, the magnitude of the magnetic flux density decreases with increasing distance from the area between the windings. To illustrate this, Figure 3.4 is a plot of the magnetic flux density, B_Z, along the z-directed axis of the coil according to the following equation:

$$B_z = \frac{\mu_0}{2} \frac{i_{RMS} N r^2}{\left(r^2 + z^2\right)^{3/2}}$$

(3.1)

where i_{RMS} is the 35mA current through the coil, N is the number of turns (32) and r is the radius of the coil (3"). In addition, Figure 3.4 also depicts the simulated value of B_z along the axis for comparison. The magnitude of B_z is at a maximum in the area within the windings of the loop/ring of wire and falls off with the cube of the distance from the center of the coil along its axis. It is clear from Figure 3.4 that the analytical expression compares quite well with the simulated results.
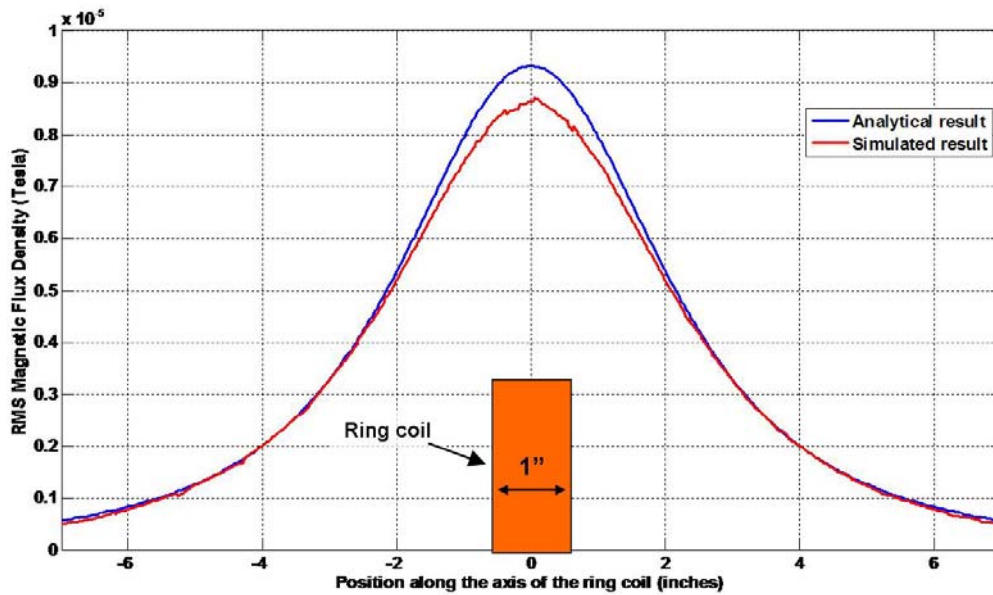
Figure 3.4: Magnitude of the normalized magnetic flux density, B_z, along the axis of a loop/ring geometry

Since it is the normal component of the vector field that contributes to the induction of eddy currents with the molten metal, this combination of divergence and decay means that as the distance between the melt and coil increases, the interaction (mutual coupling) between them will decrease and the coil will be less sensitive to the presence of the metal.

3.2 Circuit Design

3.2.1 Oscillator

Figure 3.5 is a schematic diagram of the Colpitts oscillator used in this system. The inductor, L_1, in the circuit is the coil described in the previous section and the capacitors C_1 and C_2 comprise the reactive voltage divider that provides feedback to the BJT amplifier.

Figure 3.5: Common-base Colpitts oscillator circuit

The primary concern when choosing the components for this circuit was to maximize the long-term stability of the oscillator when operated over a range of conditions, includin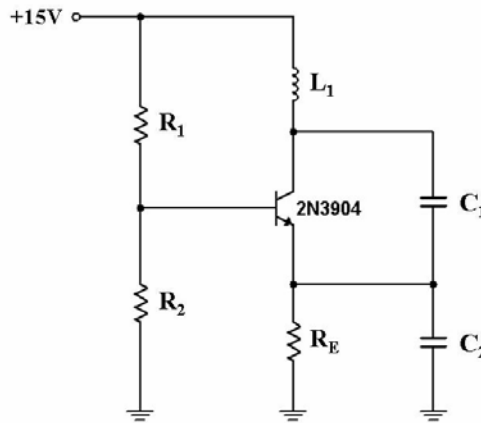g temperature fluctuations, component variations, etc. If the oscillator's stability is susceptible to these variations, the repeatability of the system will be compromised and its overall performance will degrade as a result. To avoid this, careful attention was paid to both the biasing of the BJT, as well as the thermal specification of the capacitors in the feedback network.

The BJT in the oscillator is biased by the voltage divider comprised of R_1 and R_2, as well as the emitter resistor, R_E. Careful consideration was given to the values of these resistors in the hope of minimizing the circuit's susceptibility to the aforementioned variations. There are two characteristics of a BJT whose values vary due to ambient temperature, as well as from one component to the next. These characteristics are the DC current gain (h_{FE}) of the transistor and the base-to-emitter voltage drop (V_{BE}), both of which can cause significant variability in the DC

operating point of the oscillator. However, if a transistor is properly biased through the appropriate selection of resistor values, the influence of the transistor's environment can be minimized.

To analyze how these parameters influence the operation of the transistor, we can derive the equations that describe the large-signal (DC) behavior of the oscillator. First, we replace the resistive bias network of R_1 and R_2 in Figure 3.5 with its Thévenin equivalent resistance, R_{TH}, and voltage, V_{TH}, given by

$$R_{TH} = R_1 \parallel R_2 = \frac{R_1 R_2}{R_1 + R_2} \tag{3.2}$$

$$V_{TH} = \frac{R_2}{R_1 + R_2} V_{CC} \tag{3.3}$$

resulting in the circuit pictured in Figure 3.6.
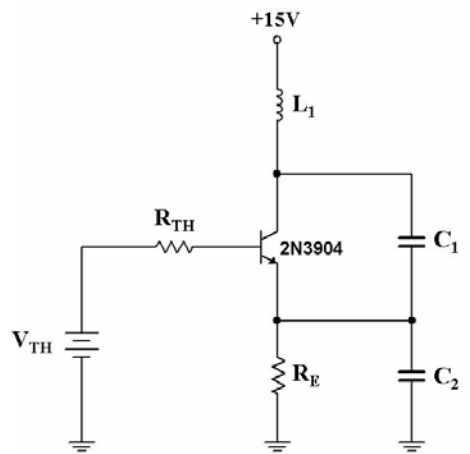
Figure 3.6: Common-base Colpitts oscillator with a Thevenin equivalent for the bias network

Second, we need to replace the BJT with its large-signal model for the active region of operation, pictured in Figure 3.7.

23
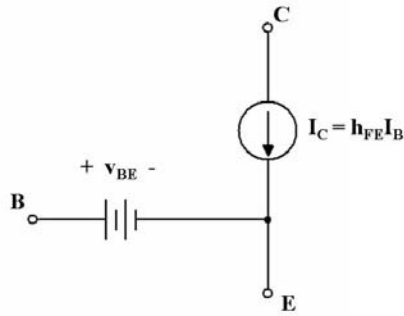
Figure 3.7: BJT large-signal model for operation in forward active region

If we combine the Thévenin equivalent circuit with the large-signal model in Figure 3.7, replace the inductance with a short circuit and capacitors with open circuits, the result is the complete large-signal circuit or the oscillator shown in Figure 3.8.
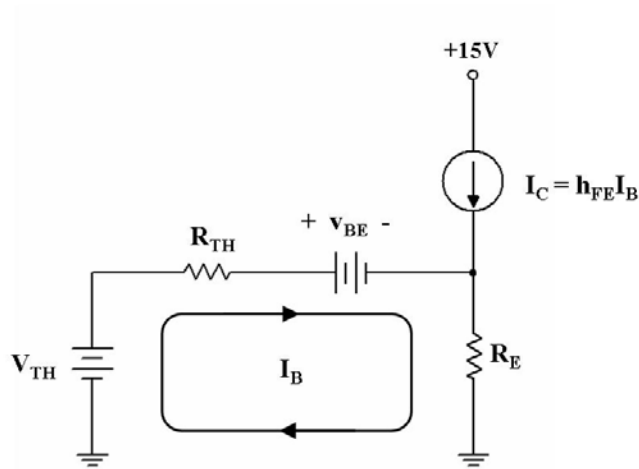
Figure 3.8: Large-signal model of the common-base Colpitts oscillator

By applying Kirchhoff's voltage law to the loop identified in Figure 3.8, as well as the fact that $I_B = I_C / h_{FE}$, we obtain the following equation

$$-V_{TH} + \frac{I_C}{h_{FE}} R_{TH} + V_{BE} + \frac{I_C}{h_{FE}} R_E + I_C R_E = 0 \qquad (3.4)$$

If we rearrange terms, we can produce an expression for I_C

$$I_C = \frac{V_{TH} - V_{BE}}{R_E\left(1 + \dfrac{1}{h_{FE}}\right) + \dfrac{R_{TH}}{h_{FE}}} \tag{3.5}$$

We now drop the $1/h_{FE}$ term in (3.5) under the assumption that $1/h_{FE} \ll 1$. Therefore, the equation for the bias collector current, I_C, is

$$I_C = \frac{V_{TH} - V_{BE}}{R_E + \dfrac{R_{TH}}{h_{FE}}} \tag{3.6}$$

To reiterate, V_{BE} and h_{FE} are the two values in the equation whose influence we would like to minimize. Let us first consider V_{BE}, located in the numerator of (3.6). If the value of the Thévenin equivalent voltage (V_{TH}) is close to the typical value of V_{BE} (~0.7V), even the smallest variations in V_{BE} could have a significant impact on the value of I_C. However, if V_{TH} is much larger than V_{BE}, the influence of these variations can be reduced considerably. In the circuit from Figure 3.5, the values of R_1 and R_2 are 220kΩ and 620kΩ, respectively. Therefore, according to (3.2) and (3.3), R_{TH} = 162.4kΩ and V_{TH} = 11.07 V. Because this Thévenin voltage is so large relative to the normal values of V_{BE} over the temperature range of interest, any fluctuations will have almost no impact on the numerator of (3.6) [14], [15].

Furthermore, the influence of h_{FE} is mitigated through the appropriate selection of these resistances. If we consider (3.6) once again, we see that if the value of R_E is selected to be larger than the ratio of R_{TH}/h_{FE}, then any fluctuations in h_{FE} will not have a significant affect on the DC operating point of the oscillator. Using R_{TH} = 162.4kΩ and assuming that h_{FE} is approximately equal to 200 based on our expected collector current of 2mA, we see that R_E should be chosen to be much larger than 812 Ω. In accordance with this criteria, the value of R_E in our Colpitts oscillator is 5kΩ [14], [15].

In addition to the biasing of the transistor, careful attention should be given to the thermal specifications of the capacitors in the tuning network. Capacitors with NPO thermal characteristics ought to be selected due to their categorization as thermally-stable over a wide range of ambient temperatures [16]. Figure 3.9 shows the thermal characteristics for various classifications of capacitors.
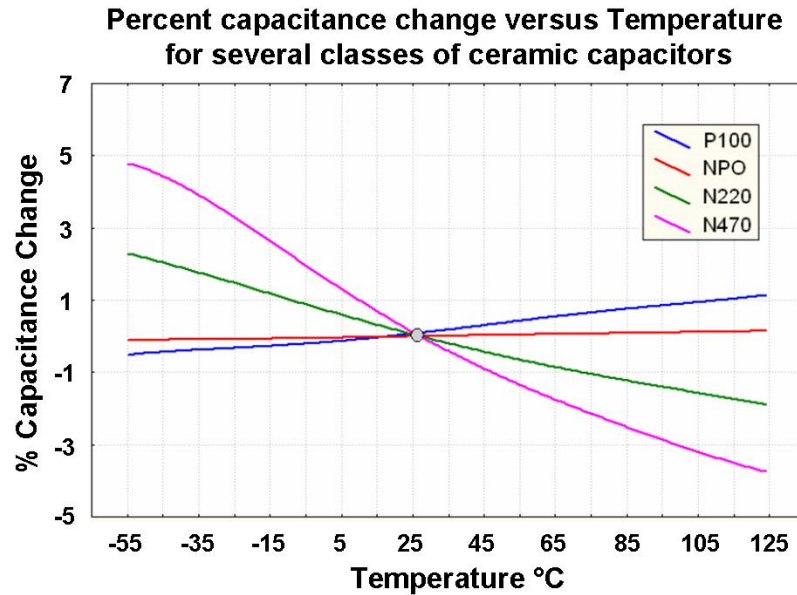
Figure 3.9: Thermal characteristic for several class I dielectrics used in capacitors [16]

As we can see, the NPO class exhibits almost no change in capacitance over the given temperature range. Ceramic capacitors with NPO temperature ratings are composed of class I dielectrics. These capacitors are primarily comprised of titanium dioxide (TiO_2) with small amounts of various ferroelectric oxides (i.e. $CaTiO_3$ or $SrTiO$) added to create temperature compensating characteristics. It is the inclusion of these components that make NPO capacitors exhibit such thermally-stable behavior [16].

With the transistor properly biased, the next step was to choose the appropriate values of C_1 and C_2 for the tuning network. To determine the values of these components, we must use both (2.36) and (2.38) to configure the circuit at the frequency we desire while ensuring that the gain requirement is met to maintain the oscillations. The expression of (2.38) dictates that based on the gain requirement of the oscillator, the ratio of C_2/C_1 should be less than or equal to 126.35. Expressed in another way, C_2 must be no larger than approximately 126 times the value of C_1.

$$\frac{C_2}{C_1} \leq g_m R = (0.0686 A/V)(1841.2\Omega) = 126.35 \qquad (3.7)$$

Given this upper bound of 126, the next question was what ration should be chosen. Smaller ratios will result in the class D amplification by the BJT in the oscillator, while larger

ratios will result in class A amplification. For this system, a ratio of $C_2/C_1 = 45$ was chosen, meaning that the amplifier would be operating in class A mode.

Based on prior experimentation with the 6" ring coil, a target frequency of 75kHz was chosen to maximize both the coupling of the ring coil to the melt and the capabilities of the signal conditioning circuitry to be discussed later on. Knowing the target frequency and the inductance of the coil ($L = 290\mu H$), as well as the appropriate ratio of the capacitive divider, we can calculate the appropriate capacitances by rearranging (2.36). Given the wide difference between the two values, the parallel combination of C_1 and C_2 in (2.36) can be approximated by C_1 alone. With all of this taken into account, an expression for C_1 is given

$$C_1 = \frac{1}{(2\pi \cdot f)^2 \cdot L} \tag{3.8}$$

After substituting values, we find that C_1 is equal to 15.53nF and C_2 is 45 times larger. Based on the availability of standard-value capacitors with NP0 thermal characteristics, a 15nF capacitor was selected for C_1, and a 680nF capacitor for C_2.

Figure 3.10 is an oscilloscope screen shot of the output waveform of this Colpitts oscillator, taken from the collector of the BJT.
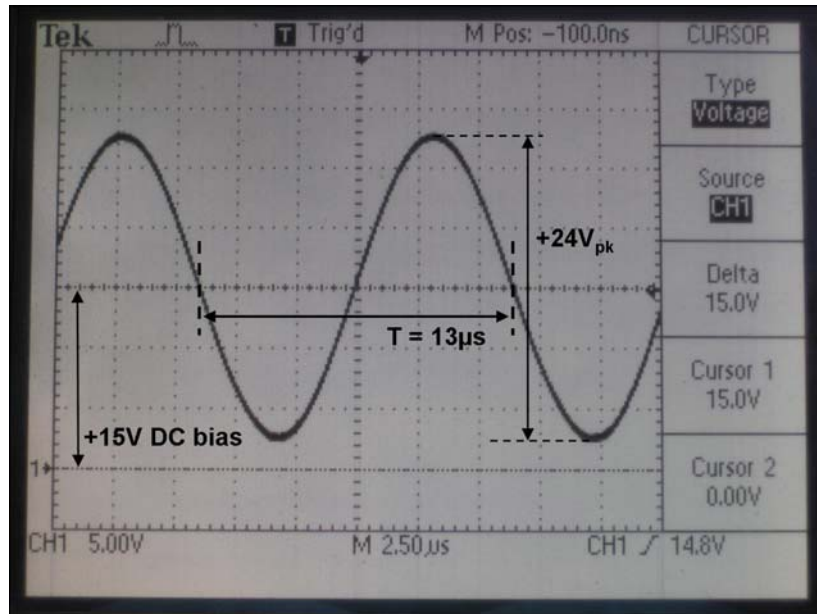

Figure 3.10: Oscilloscope screen-shot of the output waveform from the oscillator

27

This signal is a sinusoidal waveform with a period, T, of 13μs and a DC bias of +15V (V_{CC}). This period corresponds to a frequency of 76.9kHz which is quite close to our target frequency of 75kHz, differing by less than 3%.

3.2.2 Signal Conditioning

The second half of the system circuitry is dedicated to converting the frequency-shift of the output waveform from the oscillator into a signal representation that can be easily acquired by a data acquisition system, such as a DC voltage. The AD650 is an integrated circuit that is usually employed as voltage-to-frequency (V/F) converter, though it can also be configured as a frequency-to-voltage (F/V) converter [17].

Figure 3.11 shows the system block diagram of how the AD650 F/V converter operates. The primary components in the diagram are a comparator, a so-called one-shot with a switch, a constant current source and an integrator.
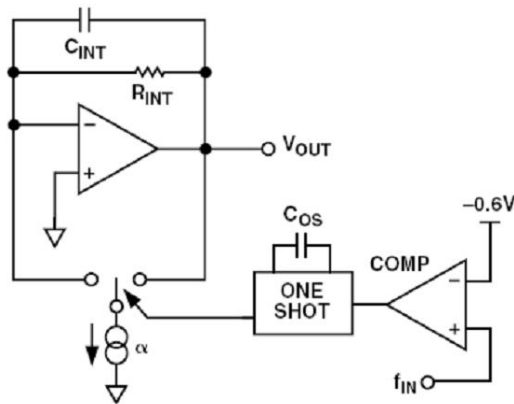
Figure 3.11: System diagram of the F/V converter [17]

The way it works is that when the input signal (F_{in}) crosses the threshold value of the comparator, the one-shot is triggered and switches the current source to the input of the integrator for a specific amount of time, t_{OS}, determined by the value of the one-shot timing capacitor, C_{OS}. The current source supplies charge to the capacitor of the integrator (C_{INT}) at the rate specified by α (coulombs/sec) until the one-shot times out and switches the current source to the output of the integrator. Since the output of the current source is a low impedance node, the

current source has no impact on the integration circuit and the current source is effectively off. Figure 3.12 is a plot of the current supplied to the integrator as a function of time. This current can be thought of as a series of charge packets occurring with frequency $F_{in} = 1/T$ at a constant amplitude of α for a specific length of time, t_{OS}.
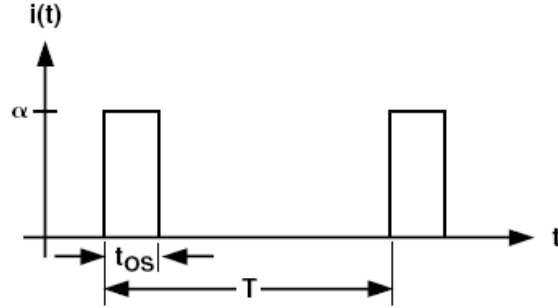

Figure 3.12: Current supplied to the integrator in the F/V converter as a function of time, t [17]

The average current supplied to the integrator, I_{avg}, can be calculated by dividing the area of the charge packet (t_{OS} x α) by the period, T. The average output voltage of the integrator, V_{outavg}, is simply the average current scaled by the integration resistor, R_{INT}, which gives

$$V_{outavg} = \frac{\alpha t_{OS}}{T} \times R_{INT} \tag{3.9}$$

If we substitute F_{in} for $1/T$, then the expression in (3.9) becomes a function of the input frequency explicitly

$$V_{outavg} = t_{OS} \times R_{INT} \times \alpha \times F_{in} \tag{3.10}$$

In practice, R_{INT} is usually comprised a fixed value resistor in series with a potentiometer to account for any discrepancies in t_{OS} and α.

To minimize the ripple in the output voltage, it is recommended that t_{OS} occupy the majority of the total period, T. As a result, t_{OS} is chosen to be 90% of the minimum period expected at the input to the converter. After choosing t_{OS}, the appropriate value for C_{OS} can be determined from the follow equation provided in [17]:

$$C_{OS} = \frac{t_{OS} - 3 \times 10^{-7} \text{ sec}}{6.8 \times 10^3 \text{ sec}/F} \tag{3.11}$$

Once C_{OS} has been determined, the value of R_{INT} can be determined from (3.10) since t_{OS}, α, F_{in} and V_{outavg} are all known (V_{outavg} is the desired DC output at the frequency of interest).

The final step is to choose the appropriate value for the integration capacitor, C_{INT}. The AD650 application note referenced in [17] advises that the time constant of the integrator be some fraction of the system response time that the chip is being used for. This ensures that the F/V converter will be able to resolve step changes in the input faster than they are predicted to occur. The equation provided to determine C_{INT} is

$$C_{INT} = \frac{SystemTimeConst.}{N \times R_{INT}} \tag{3.12}$$

where larger values of N will yield faster settling times and increased accuracy [17].

Figure 3.13 is a detailed connection diagram of the AD650 configured as an F/V converter. The first step in choosing the appropriate components for a given application is to calculate t_{OS} based upon the maximum expected frequency of F_{in}. Since the Colpitts oscillator is designed to have a natural frequency around 75kHz, a maximum expected frequency of 80kHz was chosen ($T = 12.5\mu s$). To incorporate an additional safety factor, t_{OS} was chosen to be 90% of the period, yielding $t_{OS} = 11.25\mu s$. Using (3.11), $C_{OS} = 1.8nF$ was selected for the one-shot capacitor.
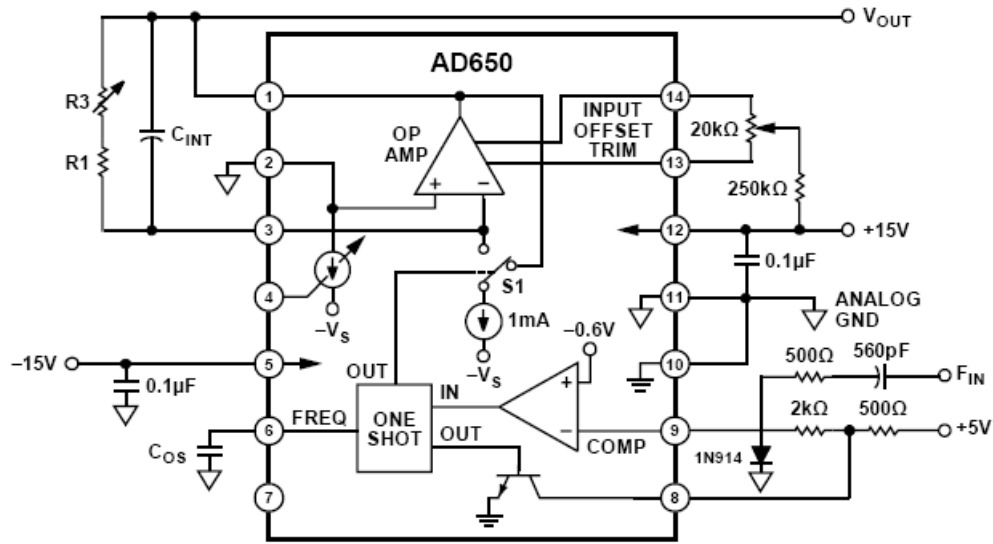
Figure 3.13: AD650 configured for operation as an F/V converter [17]

The next step was to determine the values of R_1 and R_3 that sum to R_{INT}. R_{INT} can be calculated from (3.10) knowing that $V_{outavg} \approx 9.5V$, $t_{OS} = 11.25\mu s$, $F_{in} = 75kHz$ and $\alpha = 1mA$. The result is that R_{INT} should be approximately equal to 11.26kΩ, meaning that resistances of $R_1 = 9.1$kΩ and $R_3 = 5$kΩ would be sufficient.

The final step was to calculate an appropriate value for C_{INT} using (3.12). Without knowing the actual response times of the casting processes for which the system might be implemented on, a worst-case value of between 1.5-2 seconds was chosen. Choosing $N = 100$ to assure that the F/V converter response time be less than that of the casting system, and having already determined that $R_{INT} \approx 11.26$kΩ, this means that C_{INT} should be within the range of 1.33-1.78μF. In our configuration, the value of C_{INT} was chosen to be 1.5 μF.

The remaining challenge is to interface the output of the oscillator with the input of the F/V converter. At its output, the signal from the oscillator is sinusoidal with a DC offset of +15V, while the input to the F/V converter requires a +5V pulse-train signal (+2.5V amplitude square wave with a +2.5V DC offset). This sinusoid from the oscillator must be conditioned into a new signal that is appropriate for the F/V converter without losing or affecting the information contained by the original waveform.

To accomplish this, a zero-crossing detector with a DC-blocking network ahead of its input was selected and implemented, pictured in Figure 3.14.
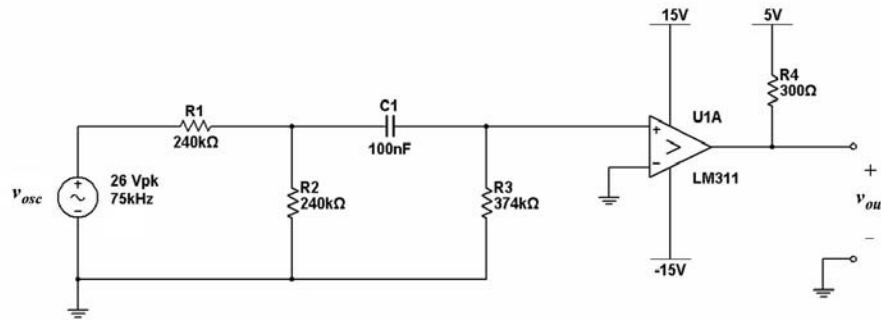
31

Figure 3.14: DC-blocking network and zero-crossing detector

The blocking network ahead of the detector will remove the +15V DC offset from the oscillator output signal so that the sinusoid does indeed cross zero as required for the detector to function properly. Furthermore, the network also attenuates the sinusoid to ensure that the input to the detector is within its ±15V input range. The detector itself is simply a comparator that produces a +5V pulse-train output with a frequency identical to that of the input sinusoid.

Let us first examine this blocking network in greater detail to better understand its functionality. The network ahead of the comparator is pictured in Figure 3.15 with the oscillator output waveform being modeled as the voltage source V_{OSC} and the eventual input voltage to the detector labeled V_{Detect}.
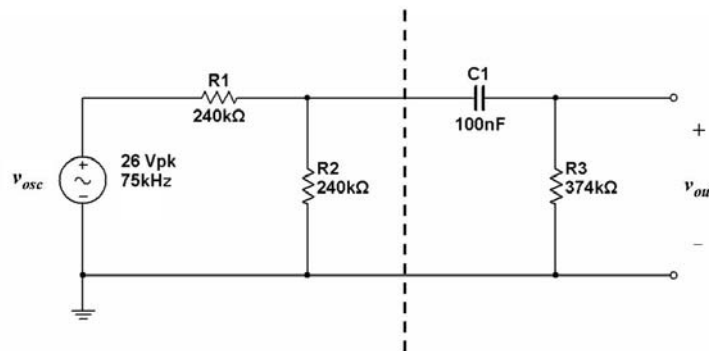

Figure 3.15: DC-blocking network

What we would like to do is derive an expression for the transfer function, H(ω), of this network and examine its magnitude and phase response over a range of potential input

frequencies. The first step is to calculate the Thévenin equivalent circuit of the voltage source V_{OSC} and resistive-divider to the left of the dashed line in Figure 3.15. Since the resistances comprising the divider are identical, the Thévenin voltage (V_{TH}) is simply half of V_{OSC} and the Thévenin resistance (R_{TH}) is the parallel combination of two 240kΩ resistors, resulting in $R_{TH} =$ 120kΩ. Figure 3.16 depicts an updated schematic of the blocking network having substituted these Thévenin equivalent elements.
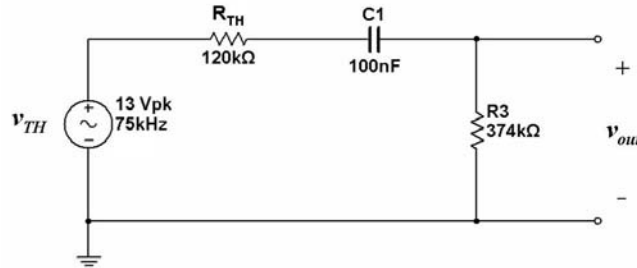

Figure 3.16: DC-blocking network with Thevenin equivalent substituted

From this simplified schematic, it can be shown fairly easily that the transfer function of this network is

$$H(\omega) = \frac{V_{OUT}}{V_{TH}} = \frac{j\omega R_3 C}{1 + j\omega(R_{TH} + R_3)C} \tag{3.13}$$

The final step is to substitute $V_{TH} = V_{OSC}/2$ to yield the final expression

$$H(\omega) = \frac{V_{OUT}}{V_{OSC}} = \frac{1}{2} \times \frac{j\omega R_3 C}{1 + j\omega(R_{TH} + R_3)C} \tag{3.14}$$

Figure 3.17 depicts the magnitude and phase responses of the transfer function in (3.14) generated in MATLAB. The important pieces of information to extract from these plots come from the magnitude response, specifically at low frequencies approaching DC and at the natural frequency of the oscillator. At frequencies approaching 0 Hz (DC), the magnitude response is steadily decreasing, indicating that only very small fractions of these frequency components are passed by the network. Therefore, we can see why this is called a DC blocking network since the magnitude response at 0 Hz is -34.5 dB.
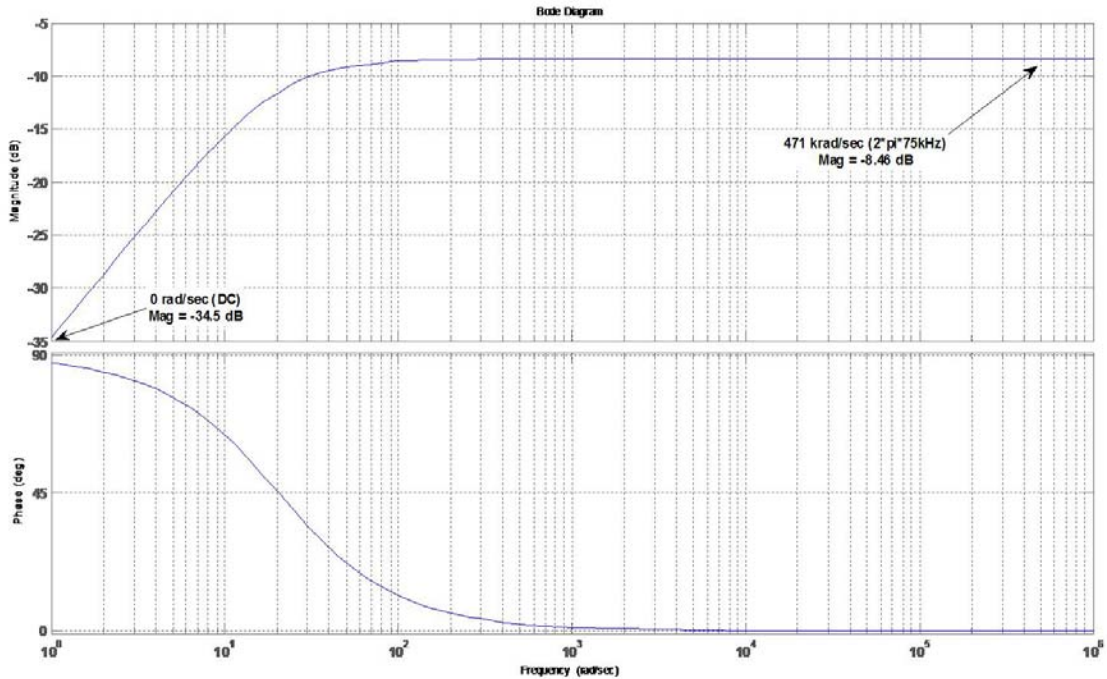
Figure 3.17: Bode magnitude and phase plots of the DC-blocking network transfer function

Furthermore, we can see that at the natural frequency of the oscillator (~75kHz or 471 krad/sec), this network should attenuate an input signal of this frequency by -8.46 dB, or by a factor of 7. In practice, the actual attenuation provided by this network upon the oscillator output signal was a factor of 12. This discrepancy between the expected and actual attenuation factors can likely be attributed to the omission of both the output resistance of the oscillator, as well as the input resistance of the comparator. If this output resistance is inordinately high (~50kΩ to 150kΩ) and/or the input resistance is abnormally low (~10kΩ to 50kΩ), the result would be a predictive attenuation factor closer to the actual value. Ultimately, the actual attenuation factor would suffice in keeping the input signal to the zero-crossing detector within the input range of the comparator (±15V). Figure 3.18 is an oscilloscope screen-shot depicting the input and output waveforms associated with the blocking capacitor.
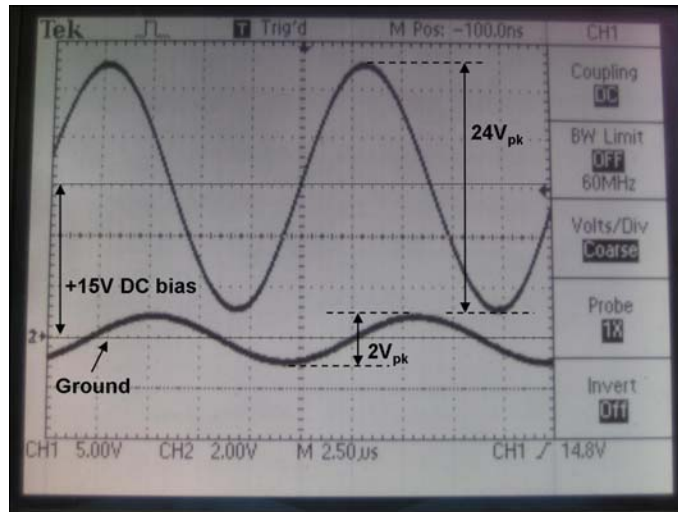
Figure 3.18: Oscilloscope screen-shot depicted the decoupling and attenuation by the blocking network

Following the blocking network in Figure 3.14 is the LM311 comparator used as the zero-crossing detector. This comparator generates a square wave version of the incoming sinusoid whose frequencies are identical to one another. As the sinusoid crosses zero with a positive slope, the output of the comparator switches to its high-state of +5V. Conversely, when the sinusoid crosses zero with a negative slope, the comparator switches to its low-state, which in our case is ground. Figure 3.19 is an oscilloscope screen-shot showing these input and output waveforms associated with this detector.
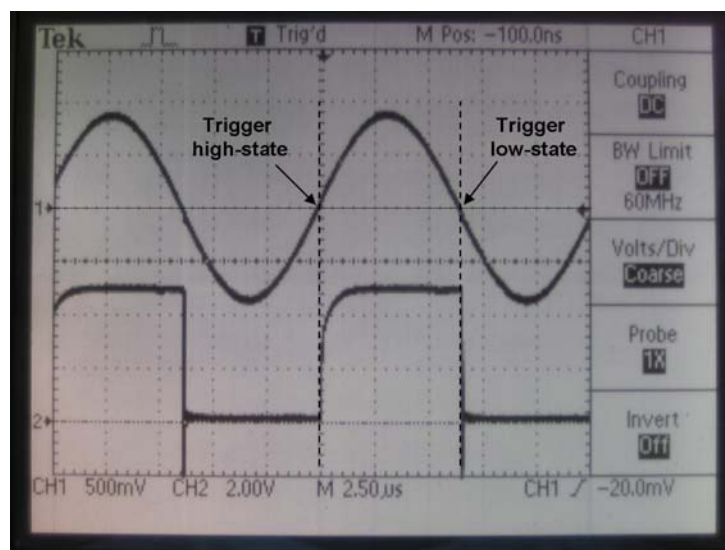

Figure 3.19: Oscilloscope screen-shot of the input and output waveforms of the zero-crossing detector

The pulse train that results at the output of the comparator is the input signal to the F/V converter that produces a DC output voltage that is proportional to the frequency of the input.

Once the performance of the system was validated on a bread-board, the design was committed to a printed circuit board (PCB) in preparation for eventual packaging and industrial testing. The first step was to capture a schematic detailing the circuit components that would be included on the PCB. All of the circuit blocks described to this point, including the oscillator, zero-crossing detector and F/V converter, were drawn-up using a schematic editor.

In addition, a separate block of circuitry was designed and included to provide the voltage buses required by the rest of the system circuitry. Pictured in Figure 3.20, this block is comprised of a transformer to step-down the line voltage, two bridge rectifiers to produce positive and negative voltage buses, and several linear regulators to provide the required voltage levels.
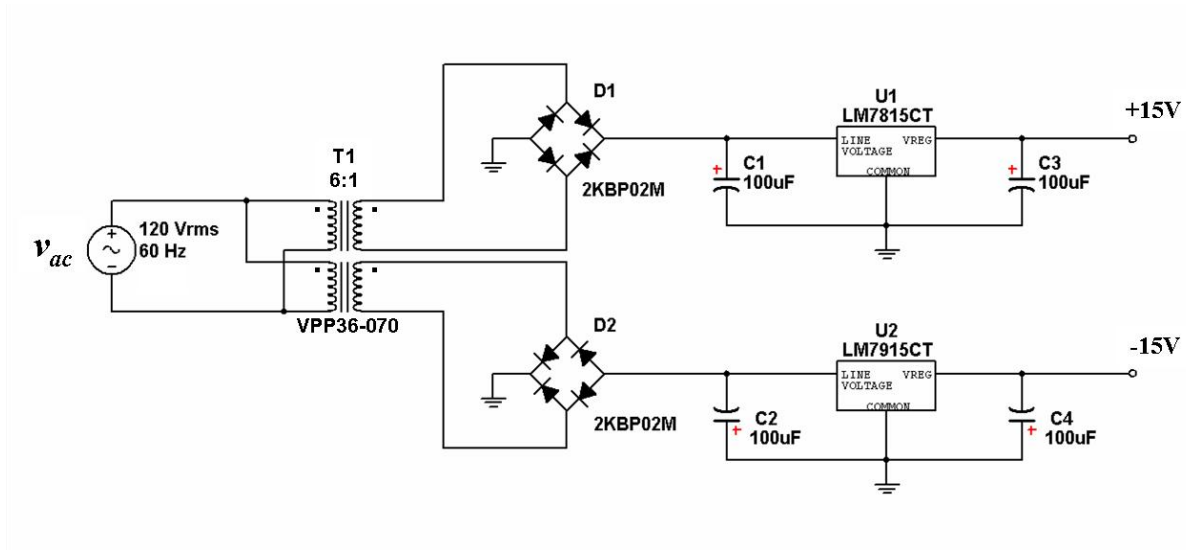
Figure 3.20: Power circuitry for PCB layout

With all of these blocks included in the schematic, a netlist detailing the interconnects amongst the components was generated by the software and exported to a layout editor. A two-layer, 0.062" thick board made of FR-4 material was selected with dimensions of 6.25" L x 3.375" W and the components were arranged with respect to their functional blocks. Once the components were placed, the traces were routed manually, utilizing both layers to exercise some control over the path and proximity of the traces with respect to one another. The widths of the ground and power traces prior to the voltage regulators was chosen to be 0.032", while the traces

for the regulated voltage buses and the oscillator were chosen to be 0.016". Lastly, all signal traces associated with the zero-crossing detector and F/V converter were chosen to be 0.008". Figures 3.21 and 3.22 are CAD images of the top (red traces) and bottom (blue traces) layers of the board layout, respectively. All of the components will be located on the top-layer side of the board.
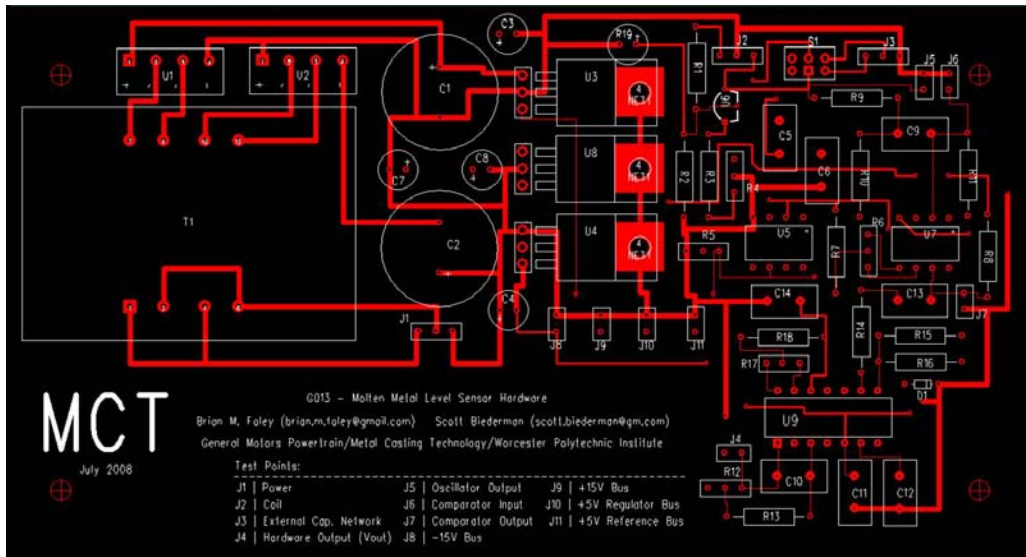
Figure 3.21: CAD drawing of the top layer PCB traces
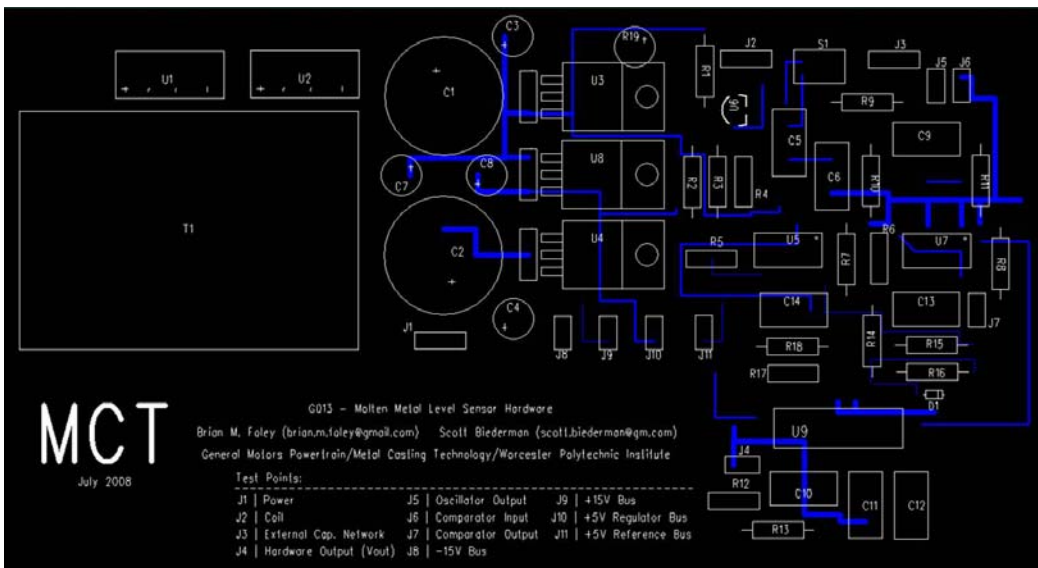
Figure 3.22: CAD drawing of the bottom layer PCB traces

Once complete, the CAD layout was then sent to a manufacturer to produce the PCB and the appropriate parts were ordered from a variety of distributors. Upon arrival, the circuit board was assembled, soldered, tested and adjusted to confirm its operation and readiness for industrial deployment. Figure 3.23 is a photo of the completed circuit board.
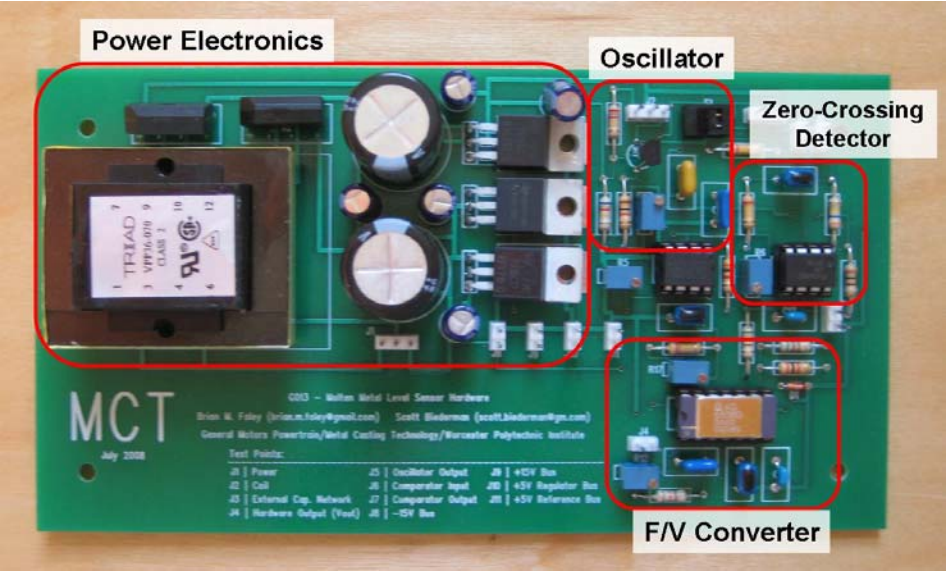
Figure 3.23: Completed system circuitry

At this point, the coil and circuitry were ready for experimental validation in a simulated casting situation to asses the capabilities of the system.

4 Experimental Validation

4.1 Methodology

To assess the performance of the overall system, a number of experiments were conducted at Metal Casting Technology, Inc. (MCT) in Milford, NH. Of particular interest was the accuracy and repeatability of the system to help the process engineers decide whether or not to deploy the sensor on their casting lines.

A total of thirty identical molds were poured at a rate of five molds per day over a three week period. For each pour, the ring coil would be located at the exact same position relative to the mold cavity, separated by 3.5" of actual sand used in precision sand casting. Each mold was wired with five k-type thermocouples (TCs) to serve as discrete indicators of metal front position for eventual comparison with the output from the sensor. In production, the inclusion of thermocouples would be impractical; they are solely intended to help validate the system's capabilities in a controlled environment.

Five discrete data points per mold from thirty molds provided 150 comparisons between the predicted position of the metal front by the coil sensor and the actual position indicated by the thermocouples. From this population of data, an isoplot can be generated using thirty random samples to assess the repeatability of the system.

4.2 Mold Design

The sand molds used in this thirty mold experiment were designed to simulate the casting of a part with a simple geometry being filled from bottom to top. The geometry was kept simple in an attempt to ensure that the thirty molds are as identical as possible, thereby minimizing any error due to mold variability.

Figure 4.1 is a drawing of the mold used in the experiment, including the location of the thermocouples and ring coil. The mold itself consists of a downsprue, runner, gate, part cavity and overfill riser. When the mold is being filled with molten aluminum, the metal is poured from a ceramic crucible into the downsprue. While in the downsprue, gravity forces the metal into the runner where it travels horizontally through the runner to the gate and enters the cavity

from below. Once the cavity is completely filled, the excess metal collects in the overfill riser and serves as a visual indicator to stop pouring.
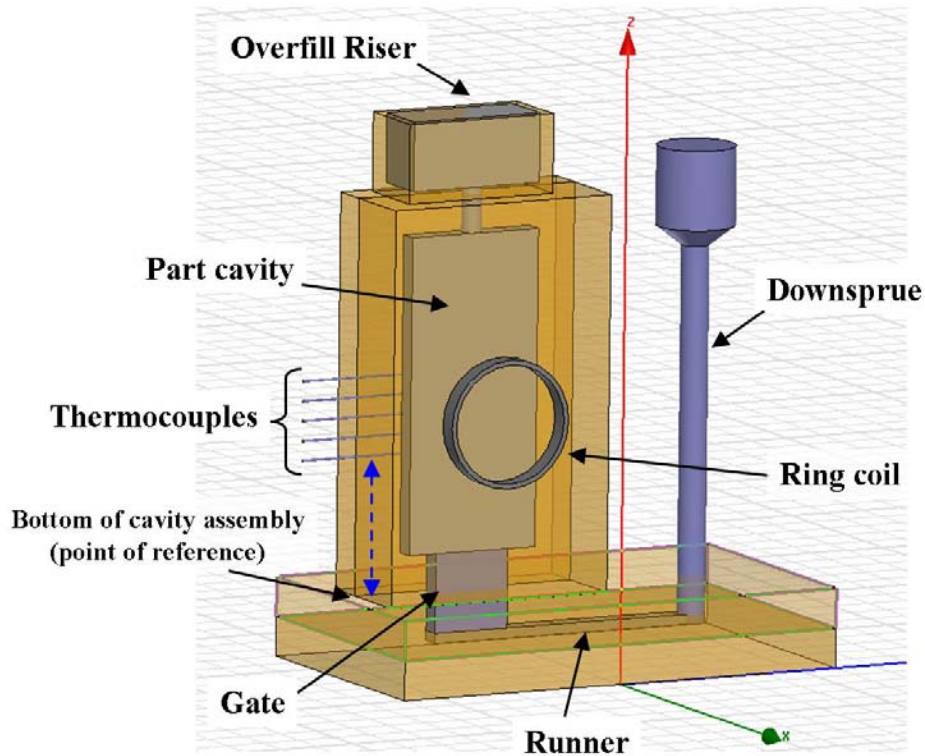

Figure 4.1: Drawing of the half-grate mold used in the 30 mold experiment

As mentioned previously, each mold is wired with five thermocouples located at specific positions relative to the bottom of the cavity assembly (see Figure 4.1, dashed blue line). The positions of the thermocouples relative to this point of reference are 7", 8", 9", 10" and 11", respectively. The thermocouples are sandwiched between the two halves of the mold cavity assembly so that they protrude approximately 0.25" into the mold cavity. Lastly, the ring coil was positioned on the exterior of the mold so that the center of the coil was located 7" from the same point of reference used for the thermocouples (the position of the coil in Figure 4.1 is not exact).

Figure 4.2 is an interior photo of the fill cavity. The regular-box geometry keeps the molten metal front at a constant distance of 3.5" from the sensor throughout the pour. Although the eventual goal is to use the sensor for more irregular surface geometries, this simple shape was used to understand the system's base-line capabilities. The dimensions of the cavity are 16.5"L x 7.125"W x 0.75"D as indicated in Figure 4.2.
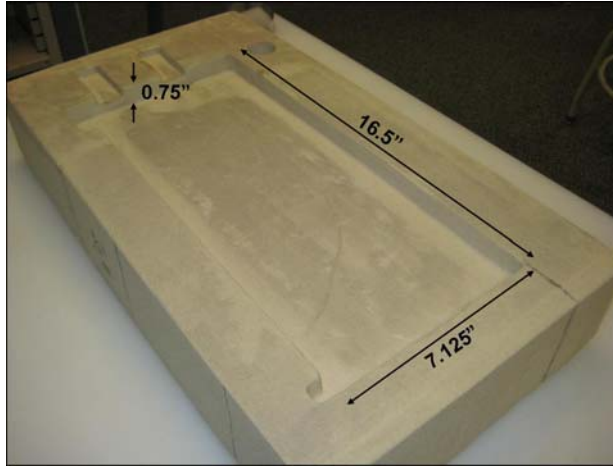
Figure 4.2: Fill cavity of the half-grate mold

The molten aluminum is fed into the cavity through the gate pictured in Figure 4.3. The placement and geometry of the gate affects the way that the cavity is filled with molten metal and can have a major impact on the material properties as and overall quality of the final casting. For our purposes, the design of the gate was not critical and a simple, rectangular structure was used to reduce the anticipated turbulent flow within the mold. The runner pictured in Figure 4.4 is a basic, horizontal channel connecting the gate and the downsprue.
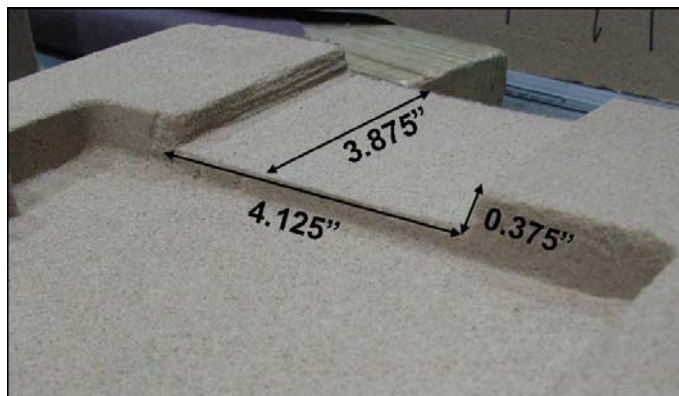
Figure 4.3: Gate of the half-grate mold connecting the runner and the fill cavity
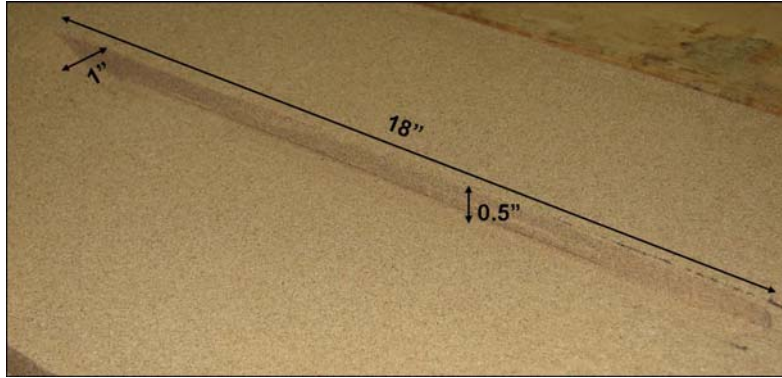
Figure 4.4: Runner connecting the bottom of the downsprue to the gate

4.3 Execution

The molds were poured at a rate of five per day, two days per week over a three week period. The pour schedule was arranged in this manner to allow for environment variability within the experiments, including temperature, humidity, power quality and concurrent experimentation/production activities. In an industrial application, a system such as this sensor would need to operate under a range of conditions. Therefore, including these sources of environmental variability is critical for assessing the sensitivity of the system to these environmental factors. An additional variable was added to the experiment by pouring the molds at different rates. In theory, this variable should not affect the accuracy of the system and may emphasize a secondary ability of the system to monitor the flow rate of the melt in addition to its position within a mold.
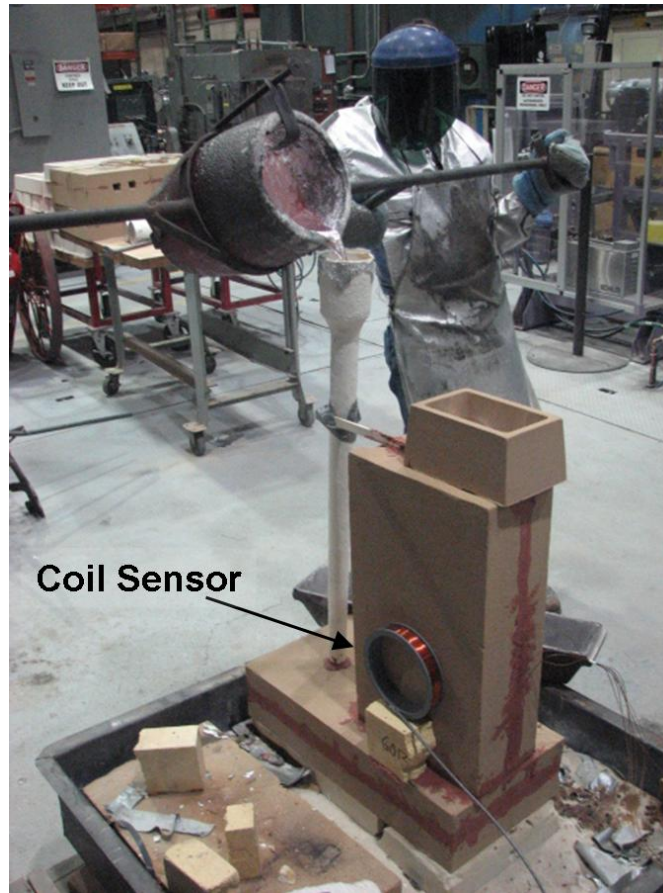
Figure 4.5: Molten aluminum being poured into the downsprue of one mold from the experiment

As each mold was being poured, the voltage signals from both the sensing system and the thermocouples (TCs) were logged by a LabView-based Data Acquisition (DAQ) system. After the acquisition was complete, the data was analyzed to determine how well the system could resolve the position of the metal front. This analysis would require the separate decomposition of both the thermocouple data and the sensor data to generate an isoplot of actual versus predicted metal-front position to gauge the accuracy of the sensor.

The first step in analyzing the data was to use the thermocouple signals to determine the exact times that the melt reached specific positions within the mold. Thermocouples were used because there should be a noticeable jump in temperature when the thermocouple comes in contact with the molten aluminum. Figure 4.6 confirms these expectations and shows the five thermocouple signals from one of the thirty molds (i.e., Mold 7).
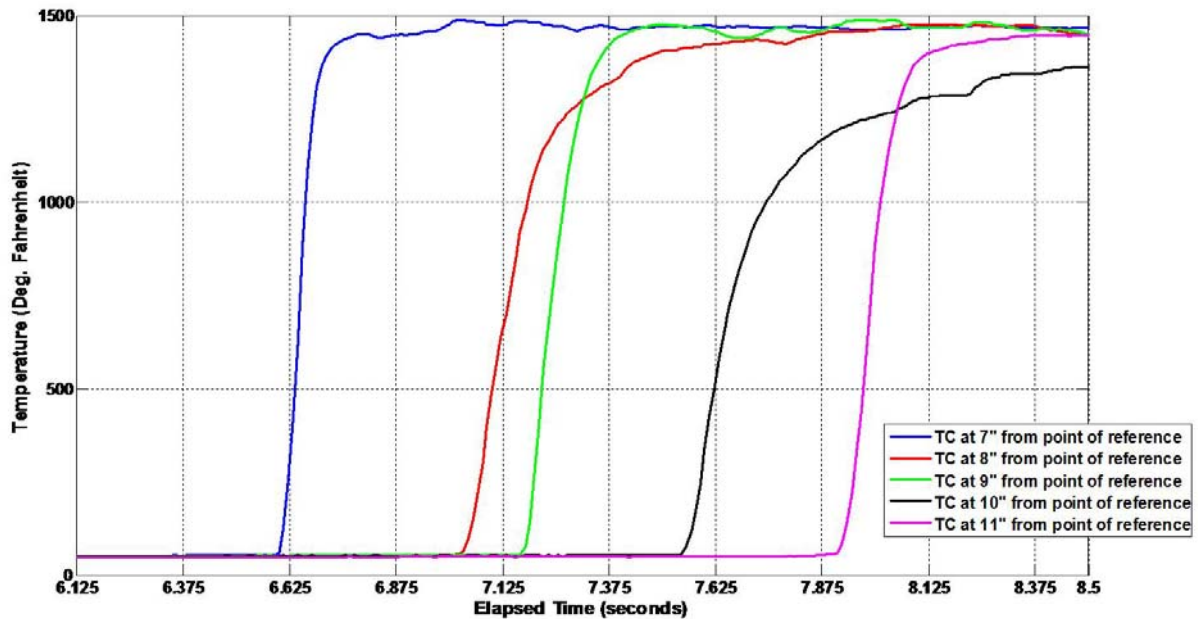
Figure 4.6: Plot of the thermocouple signals from Mold 7

The problem with using thermocouples for this purpose is that while the response is very noticeable, it is not instantaneous. Instead, there is a short delay between when the metal touches the thermocouples and when it settles at the actual temperature. This delay is due to the thermal time-constant of the thermocouples which dictates how the device will respond to an impulse of temperature change. To account for this delay, it was decided that a thermocouple would be assumed to be in contact with the metal after the first perceptible jump in temperature had occurred between two consecutive samples. Figure 4.7 is a close-up of the signal response from the thermocouple at the 11" position from Mold 7 to illustrate this methodology.
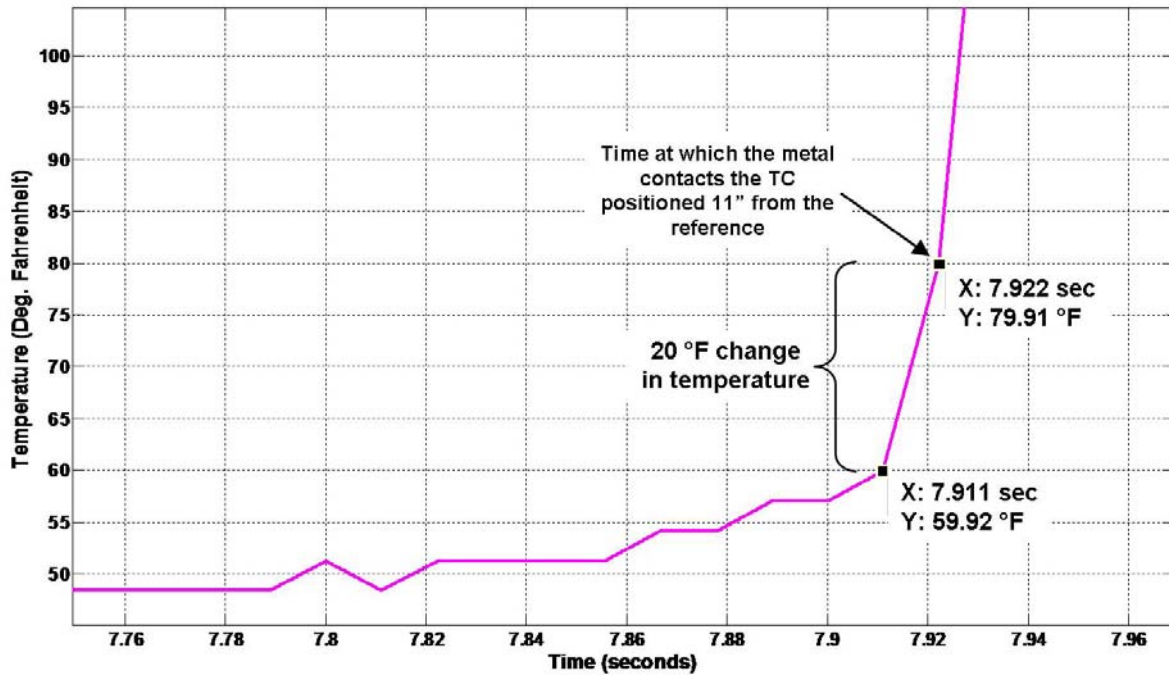
Figure 4.7: Close-up of the signal from the 11" thermocouple of Mold 7

Between the samples acquired at 7.911 and 7.922 seconds, there is a 20°F change in temperature. Since this is the first large change in the output from the thermocouple, the 7.922 second sample is assumed to be the time at which the molten metal physically contacts the thermocouple positioned 11" from the point of reference. This same concept was employed for all the thermocouple signals in the experiment. The increase in temperature prior to the 7.911 second sample is likely due to the presence of hot air preceding the metal front.

Knowing the times that the metal had reached the thermocouples, the next step was to determine the position that the sensor would have provided at these same instants. To accomplish this, a method of calibration was necessary so that the DC voltage output from the sensor could be shifted and scaled to represent metal-front position.

The apparatus in Figure 4.8 was created to simulate a molten metal-front. While acquiring data from the sensor, the aluminum plate shown in the figure is moved into the coil's field-of-view at a constant speed of 1.4 inches per second. The dimensions of this aluminum plate are identical to those of the fill cavity within the sand molds, except for its thickness (1/8"): 16.5"L x 7.125"W.
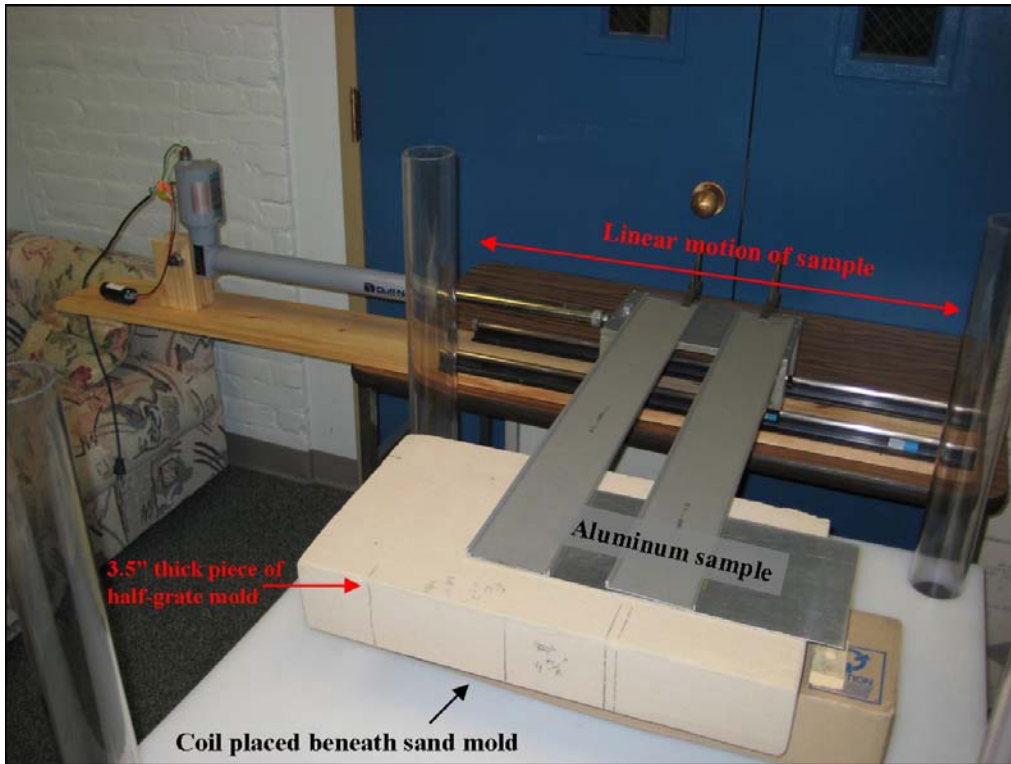
Figure 4.8: Apparatus used for calibrating the system for the 30 mold experiment

Once the acquisition is complete, the sensor signal logged by the DAQ is augmented by multiplying the time scale by the speed of the sample. The result of this multiplication is that the voltage versus time data set is converted to voltage versus metal position. The inverse of this plot (position versus voltage) is exactly what is needed as a calibration standard for the remaining thirty molds.

Figure 4.9 shows this plot of metal position versus voltage, as well as the 7th degree polynomial fit generated by MATLAB from one such calibration run. The coefficients listed in Figure 4.9 define a polynomial fit that can be used to convert the voltage output from the sensor signal into appropriate metal-front positions.

$$y = P_1 \cdot x^7 + P_2 \cdot x^6 + P_3 \cdot x^5 + P_4 \cdot x^4 + P_5 \cdot x^3 + P_6 \cdot x^2 + P_7 \cdot x^1 + P_8 \qquad (4.1)$$

where P_1 = 8.219e-4, P_2 = -4.979e+6, P_3 = 1.093e+8, P_4 = -9.202e+8, P_5 = -1.692e+9, P_6 = 8.450e+10, P_7 = -5.526e+11 and P_8 = 1.201e+12.

Figure 4.9: Plot of aluminum position versus sensor output voltage for calibration run #4

As an example, consider the sensor signal from mold 7 shown in Figure 4.10 (this mold is the same one that was used earlier when describing the decomposition of the thermocouple signals).
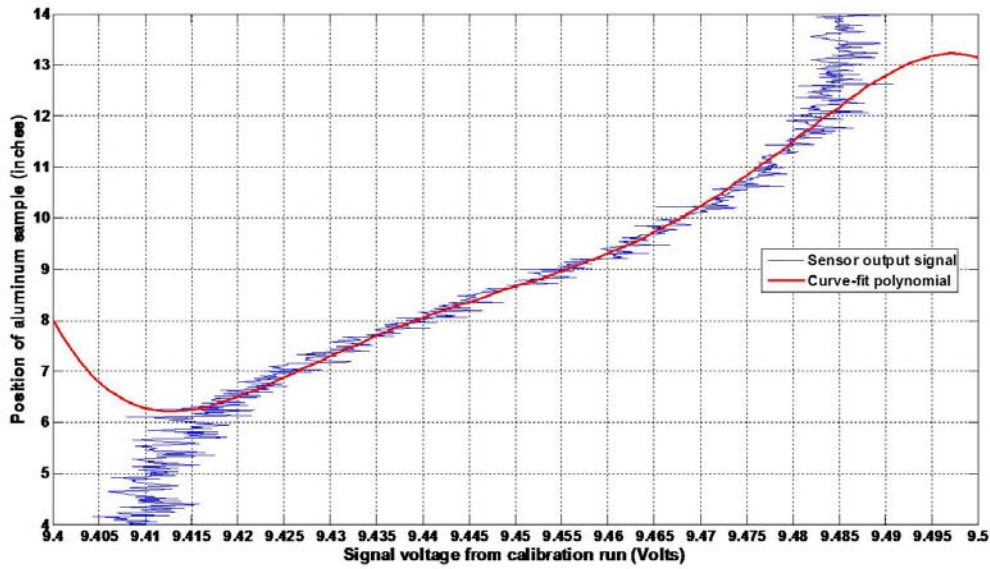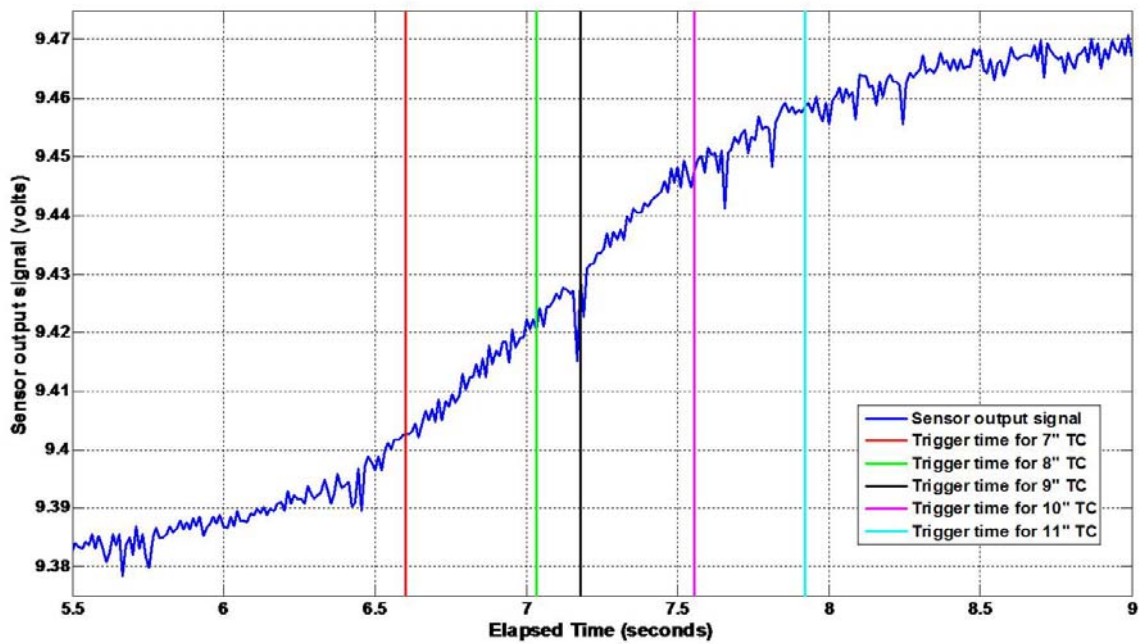

Figure 4.10: Plot of the sensor output signal and thermocouple traces/trigger times

First, the sensor output is captured at the same instant that the thermocouples come in contact with the metal. Next, the polynomial fit obtained earlier is used to convert those voltages to positions based upon the calibration standard. Finally, these positions are subtracted from the positions of the thermocouples to obtain the difference between the two. For this particular mold, the times, ideal positions and predicted positions are organized in Table 4.1.

Table 4.1: TC trigger times, actual and predicted metal front positions, and the error for Mold #7

Thermocouple trigger times (seconds)	Thermocouple positions (inches)	Predicted position by sensor (inches)	Measurement error (inches)
6.600	7	7.092	0.092
7.033	8	8.257	0.257
7.178	9	8.751	0.249
7.556	10	10.141	0.141
7.922	11	11.411	0.411

This procedure was conducted for all thirty molds, resulting in 150 comparisons of predicted versus actual metal front position (5 comparisons per mold). From this pool of 150 data points, 30 points were randomly selected to generate an isoplot and observe the repeatability of the system. This isoplot is shown in Figure 4.11. The horizontal axis corresponds to the fixed positions of the thermocouples while the vertical axis referrers to the metal-front position from the sensing system. The 45° line in the plot represents the best-case scenario where the sensor and thermocouples detect the metal at the exact same times and agree perfectly. When the 30 points are added to the plot, we see that there is measurable deviation between the data points and the ideal line.
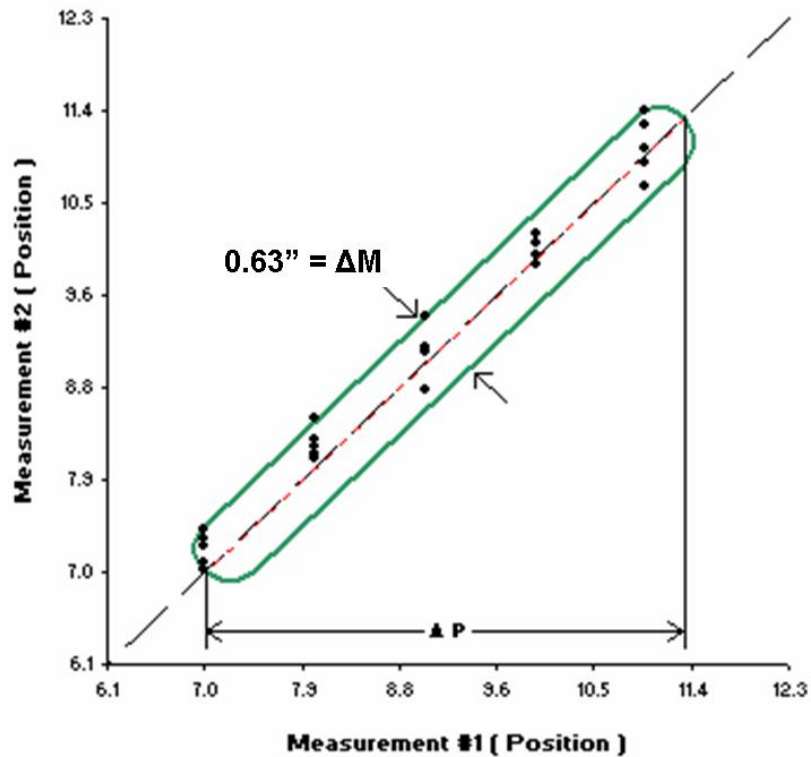
Figure 4.11: Isoplot of 30 random samples from the 30 mold experiment

To determine the total measurement error, ΔM, of the system, the procedure is to find the second-furthest data point from the ideal line and draw a limit line through this point that is parallel to the ideal line. Next, a mirror-image of this limit line is drawn on the alternate side of the ideal line to create a set of boundary lines. Lastly, the ends of the area between the boundary lines are capped with semi-circles of radius equal to $\Delta M/2$. The resulting geometry is the green line in Figure 4.11. The distance between the boundary lines is the metric 'ΔM' that represents the total measurement error of the system with 95% confidence (because the boundary lines contain 29 of the 30 samples). For the plot in Figure 4.11, the total measurement error is 0.63", giving the sensing system a statistical accuracy of ± 0.315" with 95% confidence.

The total measurement error could be attributed to a variety of individual sources. Two of these sources may have come from the calibration apparatus described earlier, including the solid aluminum target sample and the linear-motor used to move the sample. Regarding the use of solid aluminum, the electrical conductivity of solid aluminum differs from molten aluminum due to both the increased temperature of the molten metal, as well as its liquid state (lack of

crystalline structure). Therefore, the eddy currents induced in the solid sample may differ from those in the molten metal enough to introduce some amount of error at the calibration phase. Furthermore, it was later determined that the noise present on the calibration signal (see Figure 4.9, blue trace) was due to the magnetic field created by the linear-motor used to move the aluminum sample. The better approach would have been to move the sample into the coil's field of view in discrete increments, make individual measurements of the DC output voltage from the system and then curve-fit the resulting data points to generate a polynomial expression for the calibration curve.

Other sources of error may be attributed to the molds used in the experiment. For example, it is extremely unlikely that all 30 molds were identical in every way, particularly when considering the placement of the thermocouples within the mold. Locating these thermocouples the slightest amount off from their intended position would contribute a significant amount of error to the accuracy of the system. Furthermore, any inaccuracies in the placement of the coil sensor on the exterior of the mold would introduce similar concerns.

As mentioned previously in the section, the timing-ambiguity associated with the thermal time-constant of the thermocouples required an approximation as to when the metal actually reached specific positions within the mold. The better option for future validation experiments would be to use contact probes instead of thermocouples to obtain an instantaneous indication of metal position.

Lastly, processing the data from the 30 molds by hand undoubtedly introduced some amount of round-off error to the calculated values. The solution to this problem for future experiments would be to streamline the processing of sensor data by creating a single computer program, thereby eliminating user input from the calculations.

4.4 Extensions

4.4.1 Block Mold Experiment

At the conclusion of the 30 mold experiment, the decision was made to test the system on an engine block mold. The primary motivation for the additional experimentation was to make a qualitative observation on the effect of the irregular geometry on the sensor output signal and

contemplate whether or not these irregularities could be detected consistently in a production application.

Figure 4.12 is a photo of the partially disassembled engine block mold used in this experiment. The complete mold package for this eight-cylinder block consists of nine individual sand cores, as well as several cast iron chills (cylinder liners and crankshaft area). To ensure a complete casting, 175 lbs of molten aluminum was prepared in a nearby furnace.

Figure 4.12: Partially disassembled engine block mold

One particular area of interest within the mold was the volume transition from the skirts to the bulk of the block, highlighted by the red rectangle in Figure 4.13. Assuming that the delivery rate of the molten aluminum to the downsprue remains fairly constant, there should be a noticeable change in the velocity of the metal front as it transitions from the skirts to the bulk. If the sensing system can detect this change in fill velocity, it could serve as an indicator of metal front position within the mold.
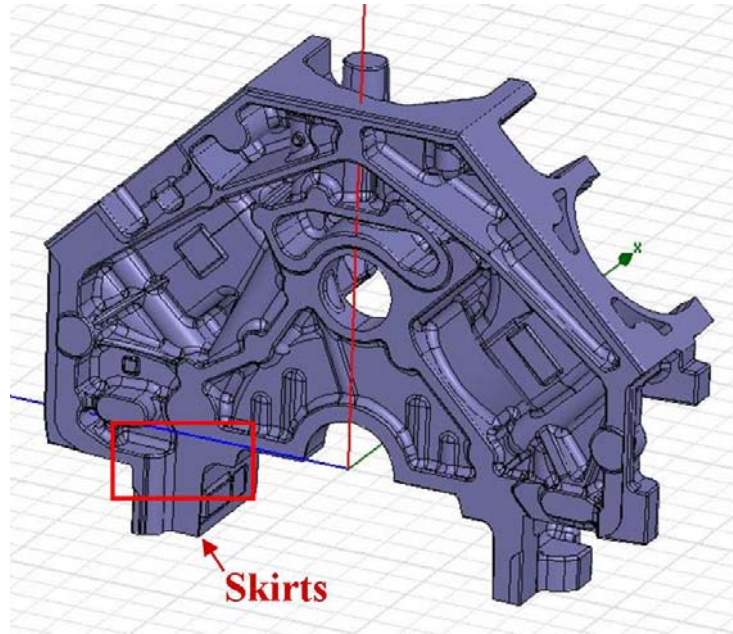
Figure 4.13: Small-to-large volume transitions between skirts and bulk of the engine block (red rectangle)

The coil sensor was positioned on the mold package so that this particular area of interest would be within its field-of-view. Furthermore, contact probes were positioned in half-inch increments along a vertical path from the skirts into the bulk of the engine block. Figure 4.14 is a photo of these contact probes protruding out from the end core of the engine block (and into the mold cavity). Contact probe #5 (circled in the photo) marks the volume transition from the skirts to the bulk of the block that is of interest to us and will provide a time-stamp to help us know where to inspect the sensor output signal for any interesting responses.

Figure 4.14: Vertical arrangement of contact probes along interior of end core

Figure 4.15 is a photo of the coil sensor placed on the exterior of the mold package. The vertical-arrangement of wires at the center of the coil are the opposite ends of the contact probes mentioned previously.

Figure 4.15: Placement of coil sensor on the exterior of the core package

In total, three engine block molds were prepared in this manner. Each mold was poured on a separate day, primarily due to the preparatory work involved and the time required to melt the 175 lbs of aluminum. Figure 4.16 is a plot of the sensor and contact probe data from one of the castings. If we focus on the area highlighted by the dashed red rectangle, we notice that there is a change in the slope of the sensor output signal near the point where the molten metal triggered the #5 contact probe. Specifically, the slope is steeper prior to the #5 contact probe being triggered and becomes shallower afterwards. This suggests that the velocity of the metal front decreased once the skirts had been filled and the metal entered the bulk of the engine block. In addition, this change in slope is quite pronounced and could serve as a fairly reliable indicator of metal front position.
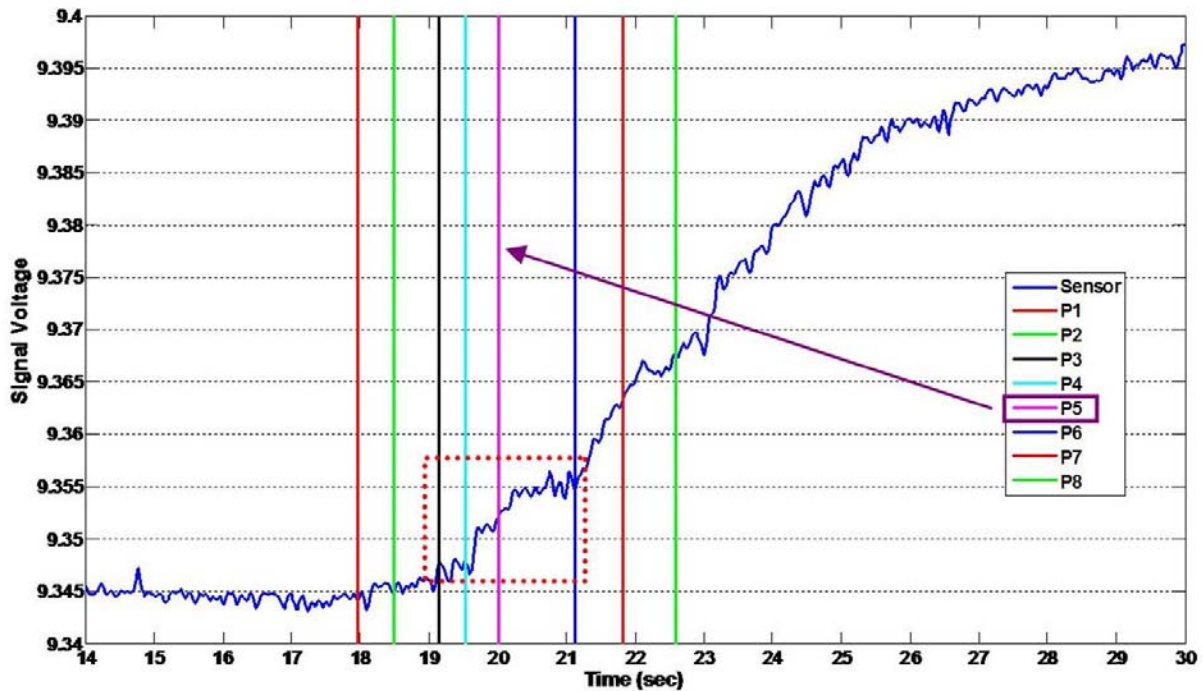
Figure 4.16: Plot of sensor output voltage and contact probe signals from block mold #1

While the system was indeed able to provide information about a large discontinuity in cavity volume, it would be much more difficult to detect the smaller features of the engine block, including surface features and smaller volume transitions. However, as molds become thinner, the system could be able to resolve some of these smaller features and provide useful information regarding their formation.

4.4.2 System Hardware and Software

Following the successful use of contact probes in the block mold experiment, the packaging of the system hardware was redesigned to incorporate an auxiliary contact probe box that would interface with the sensor enclosure and relay the data to the computer. Figure 4.17 depicts these pieces of hardware, including the contact probe box (black) and the sensor enclosure (silver).

Figure 4.17: Updated system hardware, including contact probe box (black)

Additionally, new software was created to streamline the processing of the experimental data and provide a graphical user interface (GUI) to the user. The code for this software was written in M-code for use with the MATLAB computing environment. Three separate files were created, including one for calibrating the system, one for acquiring and scaling data based on a calibration standard, and one for statistically analyzing a population of data points. Figure 4.18 is a screen shot of the user interface from the calibration software.
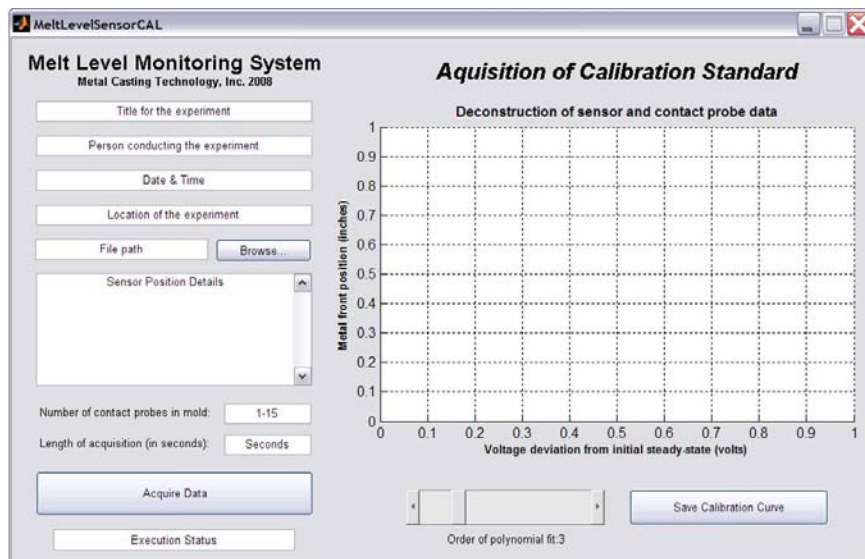

Figure 4.18: Screenshot of calibration software GUI

5 Project Conclusions

5.1 Summary

Based on the results of the experiment, the molten-metal level sensing system is well suited for determining the position of an aluminum metal-front within a 3.5" thick precision sand mold to within ±0.315" of its true position. It can be inferred from these results that the system could be used on molds made of similarly non-metallic materials (ie, ceramic) thinner than 3.5" with equal or better accuracy. Furthermore, when used with molds thinner than 3.5", the viewing range of the sensing system will expand to provide better coverage of the mold cavity being cast. Conversely, we can expect the accuracy of the system to be worse than the ±0.315" margin, and for the viewing range to be limited when used on molds with thicknesses greater than 3.5".

Although the mold used for the experiment simulated a flat surface geometry, the system could be used for casting parts with curved or irregular surfaces where the distance between the melt and the coil may vary spatially. The key to maintaining the accuracy of the system when used with these types of geometries lies with the calibration method. Therefore, one possible approach would be to create a calibration mold of the part and place several contact probes at various positions of interest along the surface closest to the coil. Once this mold is cast, the position data from the contact probes could be compared to the sensor output voltage and the result would be a calibration curve of sensor voltage versus metal position. To resolve even the smallest surface discontinuities, the contact probes should be placed extremely close together and the thinnest possible wire should be used for the probes.

Regarding the intended application of this system, the sensor may be able to provide a reasonably accurate indication of metal front position over a limited range within the 6" thick precision sand mold of an engine block. Due to the thickness of the mold and the irregular surface geometry of the block, error margins of ±0.5" to 0.75" could be expected from the current system. These margins may be unacceptable based upon the criteria required by the manufacturing engineers to improve their processes. However, while the current system may not provide a solution to the problem at hand, subsequent mold designs with thinner sand shells would provide excellent opportunities to take advantage of this technology.

Overall, the system has been developed to a point where both the ring coil and the system circuitry would be ready for deployment in an industrial environment, either as a research tool or on a production line. It is designed to withstand the harshness and variation present in a foundry environment, and has been tested within such an environment to confirm these capabilities. To protect the design and applicability of the system, a patent application has been submitted for this technology.

5.2 Recommendations

There are several recommendations that can be made to improve upon the current melt-level monitoring system. A few of these recommendations have already been mentioned within this thesis, including the creation of a computer program for processing the experimental data. This program would not only eliminate any human error in the calculations, but the user interface to the program could encompass a standardized data display to help the user make meaningful sense of the data.

In addition, an alternative method of calibrating the system for use with various mold geometries was introduced. This method would fill an actual mold with molten metal and generate a set of discrete data points using contact probes to produce a sensor voltage versus metal position curve that can be used for calibration purposes. Employing a highly accurate calibration method will be critical if the system is expected to provide useful information, particularly when applied to complicated part geometries.

The next recommendation concerns the design of the ring coil. Depending upon the application, it would be advisable to lengthen the coil to create a more solenoidal geometry. Doing so would encourage the magnetic field to emanate further out in the axial direction before looping back to the opposite end of the solenoid, thereby coupling more magnetic energy to the melt and ultimately increasing the sensitivity of the coil. In conjunction with elongating the coil, the diameter of the coil could be increased to widen the effective aperture of the coil at a given liftoff of interest. However, it should be mentioned that the implementation of a larger diameter coil will only succeed if the metal-front is known to remain horizontally flat throughout the fill process.

Another recommendation would be to adjust the parameters and components of the Colpitts oscillator to increase the current through the coil. An increase in this current could translate to an increase in the magnitude of the magnetic flux density in the region surrounding the coil, thereby creating larger eddy currents in the molten aluminum and eliciting a larger system response.

Lastly, I would recommend that the engineers and technicians experiment with the system to discover additional uses for this technology. There are so many parts being made with not only the precision sand process, but other processes involving non-metallic mold structures. The melt-level monitoring system is designed to be reconfigured for use with various types and shapes of coils as new applications come about. Once the inductance of a new coil has been measured, the capacitive network of the oscillator must be augmented to keep the natural frequency below 80kHz and the emitter resistance much be adjusted to keep the collector voltage from distorting. Once this is complete, the system is ready to be deployed as presented in this text.

6 Works Cited

[1]   J.V. Wert, "Precision Sand Casting," [Online Document], Available at HTTP: http://www.moderncasting.com/MoreInfo/0206/MoreInfo0206.pdf

[2]   Kalpakjian, S; Schmid, S., Manufacturing Engineering and Technology: Fourth Edition, New Jesey: Prentice Hall, 2001. *Sand Casting*, *pgs 264-271*.

[3]   Libby, H. Introduction to Electromagnetic Nondestructive Testing Methods: Krieger Publishing Company, June 1979.

[4]   Shull, P. (editor), Nondestructive Evaluation; Theory, Techniques and Applications: Marcel Dekker, Inc., 2002.

[5]   "Basic Principles of Eddy Current Inspection," [Online Document], Available at HTTP: http://www.ndt-ed.org/EducationResources/CommunityCollege/EddyCurrents/Introduction/IntroductiontoET.htm

[6]   Cartz, L., Nondestructive Testing: ASM International, 1995. *Eddy Current Inspection*, *pgs 173-187*.

[7]   F.T. Ulaby, Electromagnetics for Engineers, New Jersey: Pearson Prentice Hall, 2005.

[8]   Juillard, J.; Pichenot, G.; Masia, A. "Semianalytical Method for Calculating the Impedance Variation of an Arbitrary Eddy-Current Probe", IEEE Transactions on Magnetics, Vol. 38; No. 5, September 2002, Pages 3448-3453.

[9]   Wismer, M. G. A Numerical Eddy-Current Imaging Formulation for the Nondestructive Testing of Metals. M.S. Thesis, WPI: May 1990.

[10]   Cheng, D. K. Field and Wave Electromagnetics: 2nd Edition. Addison-Wesley, 1989.

[11]   Strauss, L. <u>Wave Generation and Shaping: Second Edition</u>. McGraw-Hill, 1960. *pgs 663-668, 677-686.*

[12]   Mauro, R. <u>Engineering Electronics, A Practical Approach</u>: New Jersey; Prentice Hall, 1989. *Example 8.4-4: Colpitt's Oscillator, pgs 570-572.*

[13]   Jaeger, R. <u>Microelectronic Circuit Design</u>: McGraw-Hill, 1997. *LC Oscillators, pgs 1033-1036.*

[14]   Thompson, M., <u>Intuitive Analog Circuit Design</u>: Oxford: Elsevier, 2006. *The Issue of Transistor Biasing, pgs 97-102.*

[15]   Hambley, A., <u>Electronics: Second Edition</u>: New Jersey: Prentice Hall, 2000. *4.5: Large-Signal DC Analysis of BJT Circuits, pgs 235-247.*

[16]   "CeramicCap.pdf," [Online Document], Available at HTTP: http://www.iihr.uiowa.edu/%7Ehml/people/kruger/Publications/ChipCenter/CeramicCap.pdf

[17]   "AN-279: Using the AD-650 Voltage-to-Frequency Converter as a Frequency-to-Voltage Converter." [Online Document] Martin, S., Available at HTTP: http://www.analog.com/static/imported-files/application_notes/75729603AN-279.pdf

[18]   "Mutual Inductance (The Basis for Eddy Current Inspection)," [Online Document], http://www.ndt-ed.org/EducationResources/CommunityCollege/EddyCurrents/Physics/mutualinductance.htm

[19]   "Depth of Penetration & Current Density," [Online Document], Available at HTTP: http://www.ndt-ed.org/EducationResources/CommunityCollege/EddyCurrents/Physics/depthcurrentdensity.htm

[20]   "Impedance," [Online Document], Available at HTTP: http://www.ndt-ed.org/EducationResources/CommunityCollege/EddyCurrents/Physics/impedance.htm

[21]   "Display - Complex Impedance Plane (eddy scope)," [Online Document], Available at
http://www.ndt-ed.org/EducationResources/CommunityCollege/EddyCurrents/Instrumentation/impedanceplane.htm

Appendices

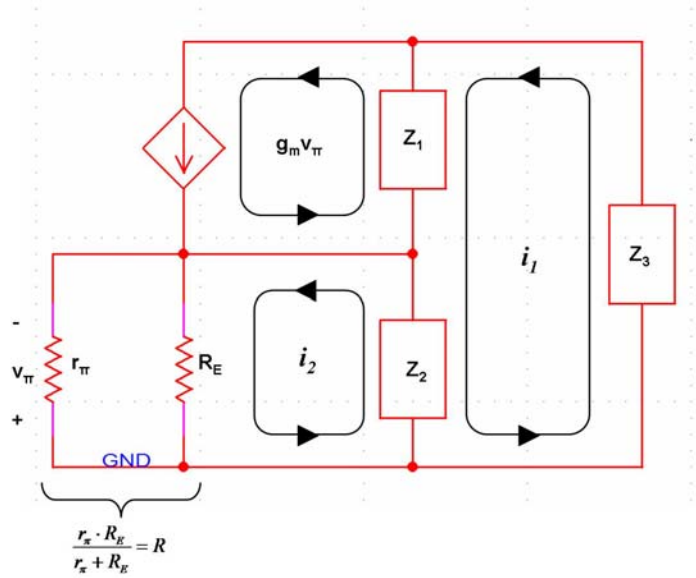## Appendix A – Derivation of Expressions for the Colpitts oscillator

Figure A.1: Small-signal model of the colpitt's oscillator used in the system

System of Equations:

$$(Z_1 + Z_2 + Z_3) \cdot i_1 + (g_m R Z_1 - Z_2) \cdot i_2 = 0$$

$$(-Z_2) \cdot i_1 + (R + Z_2) \cdot i_2 = 0$$

In matrix form:

$$\begin{bmatrix} Z_1 + Z_2 + Z_3 & g_m Z_1 R - Z_2 \\ -Z_2 & R + Z_2 \end{bmatrix} \cdot \begin{bmatrix} i_1 \\ i_2 \end{bmatrix} = \begin{bmatrix} 0 \\ 0 \end{bmatrix}$$

Calculate the determinant of the 2x2 coefficient matrix:

$$\Delta = Z_1 Z_2 \cdot (1 + g_m R) + Z_1 Z_3 + R \cdot (Z_1 + Z_2 + Z_3)$$

Separate terms into real and imaginary parts:

$$\Delta_{Real} = Z_1 Z_2 \cdot (1 + g_m R) + Z_1 Z_2$$
$$\Delta_{Imaginary} = R \cdot (Z_1 + Z_2 + Z_3)$$

Substitute the appropriate expressions for the complex impedances:

$$Z_1 = \frac{1}{j\omega C_1}$$

$$Z_2 = \frac{1}{j\omega C_2}$$

$$Z_3 = j\omega L$$

The expressions for the real and imaginary parts of the determinant become:

$$\Delta_{Real} = \omega^2 L C_2 - g_m R - 1$$

$$\Delta_{Imaginary} = R \cdot \left(\frac{1}{j\omega C_1} + \frac{1}{j\omega C_2} + j\omega L \right)$$

If we set the imaginary part of the determinant equal to zero and solve for ω, the result is the expression for the natural frequency of the oscillator:

$$\omega_o = \sqrt{\frac{C_1 + C_2}{L C_1 C_2}} = \frac{1}{\sqrt{L C_{parallel}}} ; C_{parallel} = \frac{C_1 C_2}{C_1 + C_2}$$
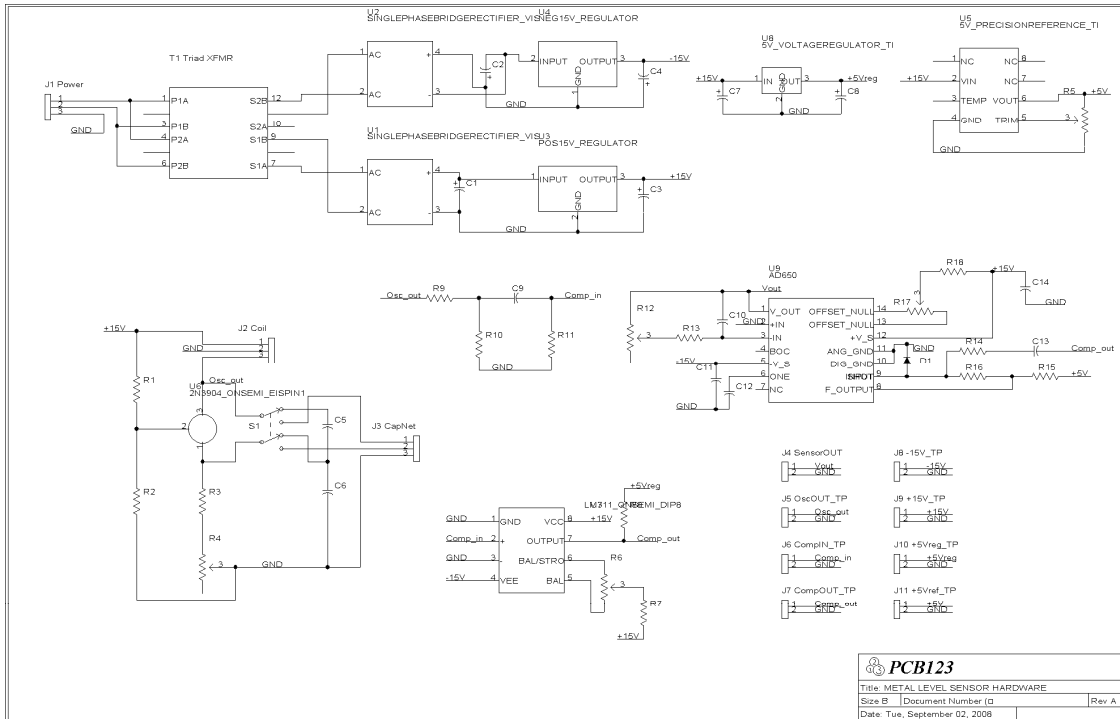
Similarly, if we set the real part of the determinant equal to zero and substitute the expression for the natural frequency, the result is the gain requirement for sustained oscillation:

$$\frac{C_2}{C_1} \leq g_m R$$

Appendix B – CAD Drawing of the Coil Former
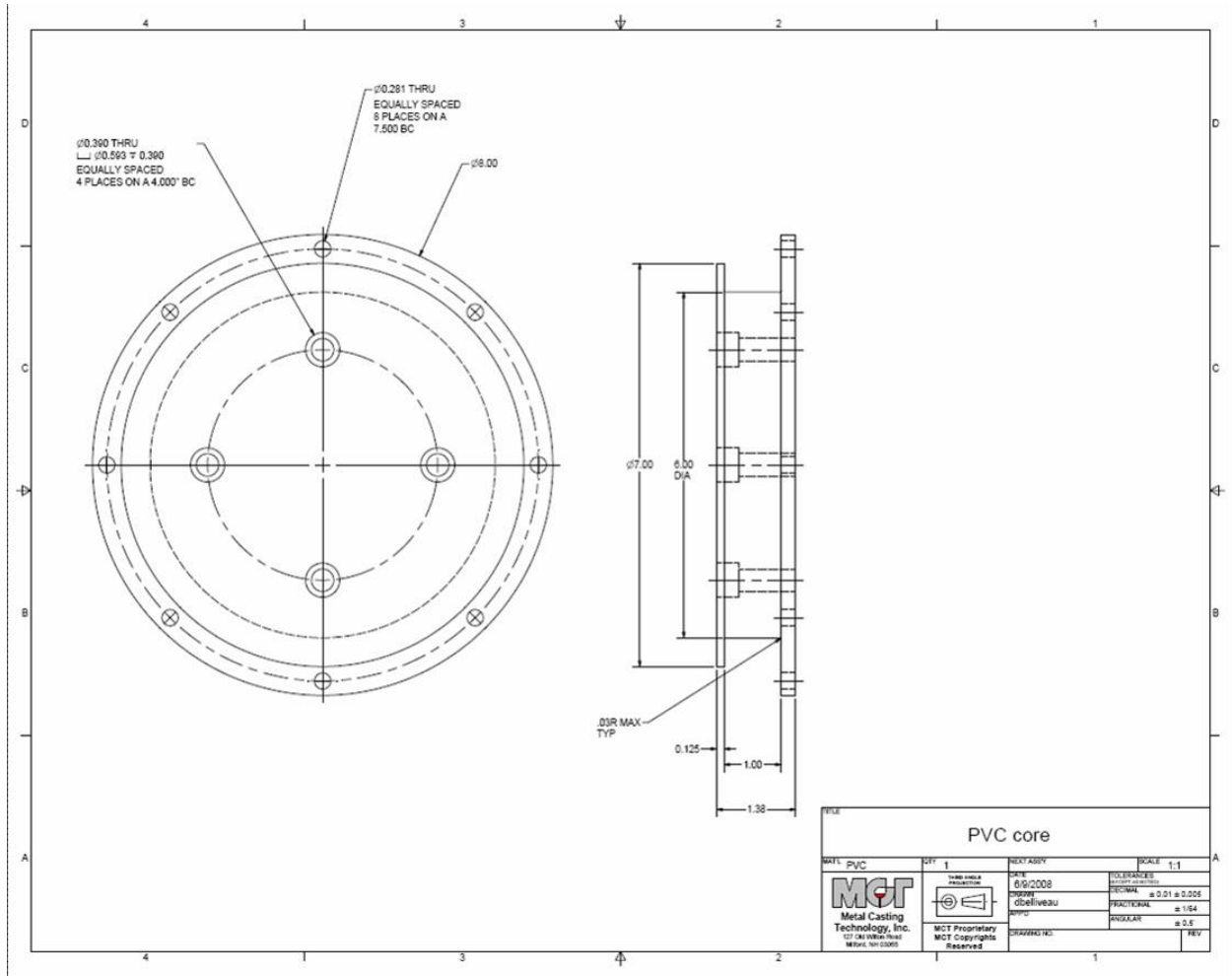
Appendix C – Complete Schematic of the System Circuitry

Appendix D – CAD drawing of Printed Circuit Board (PCB) Layout